# On the Comprehensive Precipitation of Hydroxyapatites Unraveled by a Combined Kinetic–Thermodynamic Approach

Corentin Reynaud, Cyril Thomas, Guylène Costentin

HAL Id: hal-03584442

https://hal.sorbonne-universite.fr/hal-03584442v1

Submitted on 22 Feb 2022

# On the Comprehensive Precipitation of Hydroxyapatites Unraveled by a Combined Kinetic-Thermodynamic Approach

Corentin Reynaud, Cyril Thomas, and Guylène Costentin*

*Sorbonne Université, CNRS, Laboratoire de Réactivité de Surface (LRS), 4 place Jussieu, 75005 Paris, France*

*E-mail: guylene.costentin@sorbonne-universite.fr

**KEYWORDS:** Calcium phosphates, homogeneous nucleation model, chemical pathways, stoichiometry, morphology, carbonates, hydrogenophosphates, *in situ* Raman, XRD, FTIR.

## ABSTRACT

The present study combines experimental and theoretical approaches to investigate the competitive precipitation of calcium phosphates (CaPs) in aqueous solution in order to understand and control both the structural and textural properties of the synthesized hydroxyapatites (HAps). Some of the precipitation reactions were followed by *in situ* Raman spectroscopy or achieved under kinetically controlled conditions. The CaP precursors of HAps were identified as a function of the precipitation pH of the medium and the order of introduction of the precursor ions in the synthesis reactor. Their formation was rationalized by calculations based on a homogeneous

nucleation model. Depending on the synthesis conditions, precipitation reaction pathways of HAps are proposed by bringing together the kinetic model developed in the present study and our previous thermodynamic model. HAps are complex materials due to the ease with which large amounts of crystallographic defects, such as carbonates and hydrogen phosphates, can be incorporated in their structure. As these defects play a key role in material sciences (bone substitute, heterogeneous acid-base catalysis, etc.), the present work also includes the analysis of the formation of these crystallographic defects in the apatitic framework, allowing a better control of their incorporation through careful selection of operating parameters.

**INTRODUCTION**

Used in dental and bone surgery, as food additive and in the manufacture of fertilizers, calcium phosphates (CaPs) are particularly versatile materials.[1] The use of hydroxyapatites (HAps) in heterogeneous catalysis[2–5] has led to a surge of interest in the development of innovative syntheses allowing to adjust the acid-base properties of their surface through their tunable composition.[6,7] From dry to wet routes, synthesis protocols reported to date provide access to the production of either pure or multiphasic CaPs with various morphologies, Ca/P ratios and surface properties.[8–10] Among wet routes, the extensively-used approach consisting in the co-precipitation of calcium and phosphate ions in aqueous solution appears as a virtuous and easy-to-set-up method.[7,11] This co-precipitation route involves the possible formation of several CaP minerals with distinct Ca/P ratios: HAp, (ideal crystal formula $Ca_{10}(PO_4)_6(OH)_2$, Ca/P = 1.67), amorphous calcium phosphate (ACP, $Ca_9(PO_4)_6$ Posner's clusters, Ca/P = 1.50),[12] octacalcium phosphate (OCP, $Ca_8(HPO_4)_2(PO_4)_4 \cdot 5H_2O$, Ca/P = 1.33), and dicalcium phosphate dihydrate and dicalcium phosphate anhydrous (DCPD and DCPA, $CaHPO_4 \cdot 2H_2O$ and $CaHPO_4$, respectively, Ca/P =

1.00). Furthermore, due to their flexible crystal structure, non-stoichiometric HAps can be obtained easily, with the accommodation of vacancies and/or the incorporation of hydrogen phosphate and carbonate defects $(Ca_{10-x-B}(HPO_4)_x(PO_4)_{6-x-B}(CO_3)_B(OH)_{2-x-B-2A}(CO_3)_A \cdot nH_2O)$ resulting in a broad composition domain and Ca/P ratios ranging from 1.50 to 1.90. [13,14] If biological HAps have been reported to be calcium deficient materials $(Ca/P < 1.67)$[15] with the incorporation of hydrogen phosphates and carbonates, synthetic HAps can be precipitated with various Ca/P ratios and defects.[16] In the field of heterogeneous catalysis, many studies have reported on the importance of the Ca/P ratio in the catalytic performance of HAps with a decrease in the surface basicity with decreasing Ca/P ratios.[4,17,18] This tunable acid-base balance associated with the peculiar ability of the apatitic framework for substitutions (alkaline earth metals, transition metals, lanthanides, etc.)[19–23] accounts for the strong interest in HAps as heterogeneous bifunctional catalysts. The design of HAps with controlled stoichiometries and optimized textural properties (specific surface areas and morphologies) is thus of primary importance in the field of material sciences. Although the use of electrochemical and hydrothermal energetic processes allow to obtain the apatitic phase with various morphologies,[24,25] the design of highly selective syntheses in terms of morphology and crystallographic defects incorporation by virtuous co-precipitation procedures in aqueous media and in the absence of organic additives[26,27] appears to be challenging.

The competitive precipitation of CaPs achieved by the dropwise addition of a calcium precursor solution into a phosphate solution or *vice versa*, hereafter referred to as Ca → P or P → Ca routes, respectively, at various pH values is commonly used, most often without any justification about the chosen experimental conditions, however. The literature in this field suffers from a lack of rationalization about the influence of the synthesis parameters on the properties of the prepared materials. In a recent study, we have developed a thermodynamic model adapted to continuous

dropwise addition syntheses that enables to distinguish the thermodynamic products (DCPA and HAp) as a function of the pH of the co-precipitation medium.[28] The importance of the synthesis route (Ca → P $vs$ P → Ca) has also been highlighted with the identification of a thermodynamic differentiation region in the 3.8–5.3 pH range at the beginning of the addition step. However, despite careful selection of the operating parameters likely to favor a thermodynamic control (a low addition rate of the precursor solution possibly associated with a subsequent aging step and moderate reaction temperatures), in some cases, this thermodynamic modelling of the precipitation of CaPs appeared to be insufficient to account for the observed differences in HAps morphologies, the amounts of hydrogen phosphate defects present in the apatitic crystallographic structure, or the presence of OCP in some samples.[28]

The present study provides further insights into the understanding of the precipitation reaction pathways of CaPs with the help of complementary kinetic data. In order to identify the nature of the reaction intermediates leading to the thermodynamically most stable products (DCPA or HAp), two sets of experiments have been carried out: (*i*) *in situ* Raman spectroscopy monitoring of the initial steps of syntheses likely to favor a thermodynamic control and (*ii*) additional syntheses performed under kinetically controlled conditions (a high addition rate of the precursor solution and absence of the aging step). The synthesized CaPs were also thoroughly characterized by XRD, $N_2$ adsorption and XRF, whereas the HAps structural defects (hydrogen phosphate and carbonate groups) were identified and semi-quantified by Raman and DRIFT spectroscopies. These experimental results associated with the development of a homogeneous nucleation model bring about additional elements for the understanding of the precipitation of HAps in aqueous medium at moderate temperatures (37–80 °C) whose precipitation mechanisms were found to proceed by nucleation, growth and solid-solid transformations. Finally, this study allows the identification of

the synthesis parameters exhibiting a predominant influence on the morphological and structural properties of the HAp materials such as the incorporation of crystallographic defects in the apatitic framework.

**MATERIALS AND METHODS**

**Material synthesis.** CaPs were obtained *via* a co-precipitation procedure using an automated reactor (Optimax 1001 synthesis workstation from Mettler Toledo, Figure S1).[28] Calcium and phosphate solutions were separately prepared by dissolving 12.81 g of $Ca(NO_3)_2 \cdot 4H_2O$ (Sigma Aldrich, purity $> 99.0$ %) and 3.74 g of $NH_4H_2PO_4$ (Acros Organics, $> 99.9$ %) in 250 mL of ultrapure water (resistivity of 18.2 MΩ × cm at 25 °C), respectively ($[Ca^{2+}]_0 = 0.22$ mol/L and $[H_xPO_4^{(3-x)-}]_0 = [P]_0 = 0.13$ mol/L). Two synthesis routes, Ca → P and P → Ca, have been considered depending on the order of introduction of the precursor ions into the reactor. The typical procedure is detailed in the case of the Ca → P route at pH 9.0 and 37 °C under kinetic control. 200 mL of the phosphate solution, adjusted at approximately pH 10 (ammonia 28 wt%, Sigma Aldrich) at room temperature, was poured into the reactor and maintained under an inert dinitrogen atmosphere. The medium was then gradually heated up to the desired reaction temperature (5 °C/min) under mechanical stirring (400 rpm). Depending on the targeted final ratio $[Ca^{2+}]/[P]$ (1.67), an appropriate volume of the calcium solution (200 mL), previously degassed by bubbling $N_2$ for 15 min, was added from a sample vial into the reactor at controlled speed (50 mL/min). During the addition step, the pH of the medium was kept constant at pH $9.0 \pm 0.3$ with the automated addition of suitable volumes of concentrated ammonia (28 wt%, Sigma Aldrich). Note that both the pH and the temperature of the reacting medium are easier to maintain constant ($\pm$ 0.2 unit of pH) with a slow addition rate (Figure S2). Once this step was completed, the content of the

reactor was collected and immediately filtered on Büchner. The obtained solids were then washed rapidly on Büchner (for about 5 min) with distilled water to remove ammonia, and ammonium and nitrate ions, and to prevent the transformation of the metastable phase(s) formed under kinetic control into more stable ones. The white precipitates were finally recovered on a watch glass and dried under ambient conditions for 12 h before being finely ground in an agate mortar. The same protocol was followed to synthesize all samples under conditions favoring a kinetic control when varying the operating parameters (pH, temperature, order of introduction of the precursors, addition rate of the precursor solution and relative concentration of the precursors).

**X-ray Diffraction.** Laboratory X-ray diffraction patterns were recorded with a Brucker D8 ADVANCE diffractometer equipped with a copper source ($\lambda_{Cu-K_{\alpha 1}} = 1.54056$ Å and $\lambda_{Cu-K_{\alpha 2}} = 1.54439$ Å) and a LynxEye detector. XRD patterns were recorded with 0.02 ° steps in the $2\theta$ range of 8–90 ° for high-angle diffraction. For low-angle XRD, a blade was added to the experimental set-up to prevent the detector from directly receiving the incident X-ray beam and, in that case, patterns were recorded with 0.02 ° steps in the 2θ range of 1–6 °. The indexation of the XRD lines of the CaP phases is reported in Table S1.

**Raman Spectroscopy.** *Ex situ* Raman spectra were collected from powders with a Kaiser Optical system equipped with a charge coupled detector (CCD) and a laser with $\lambda = 785$ nm ($P = 12$ or 25 mW, resolution $= 4$ cm$^{-1}$, accumulation time $= 30$ s and 30 scans per spectrum). Poorly crystalline powders were analyzed with a laser power of 25 mW instead of 12 mW to improve the signal-to-noise ratio, without any noticeable observation of material degradation. Assignment of the Raman bands of the CaP phases is provided in Table S2.

*In situ* Raman spectroscopy was performed to monitor the precipitation of CaPs in an open system for syntheses performed at pH 6.5 and 9.0, at 80 °C and following the Ca → P route with an addition rate of 2.2 mL/min. These experiments were performed using the same Raman spectrometer as that used for the *ex situ* measurements with an additional probe including an optical fiber equipped with a sapphire optical lens. The Raman probe was adapted into the synthesis device (Figure S1) so as to immerse the optical lens into the reaction medium. During the Raman measurements, the experimental set-up was maintained in the greatest darkness. The acquisition parameters were optimized to achieve the best compromise between the quality of the spectra and the acquisition time ($P = 380$ mW, resolution $= 4$ cm$^{-1}$, accumulation time $= 30$ s and 10 scans per spectrum).

**N$_2$ Sorption.** Specific surface area measurements (SSA) were carried out on a BELSORP-max instrument (BEL Japan) at 77 K after evacuation of the samples at 140 °C for 12 h under vacuum. This specific surface area was estimated by using the BET method in the $0.05 < p/p^0 < 0.30$ domain.

**X-ray Fluorescence Spectroscopy.** The Ca/P bulk ratio of the prepared CaPs was determined following the protocol described in our previous study.[28]

**Diffuse Reflectance Infrared Fourier Transform Spectroscopy.** Diffuse reflectance infrared Fourier transform (DRIFT) spectra were recorded using a TENSOR II spectrometer (Bruker) equipped with a MCT detector. About 10 milligrams of the sample was placed inside a heated crucible located in a Thermo Spectra-Tech high-temperature cell equipped with ZnSe windows. In order to eliminate the contributions of surface carbonate species (ascribed to $CO_2$ chemisorption on the basic HAp surfaces) [29] and only probe the carbonates located in the bulk, the spectra have

been recorded at 150 °C after an *in situ* thermal treatment up to 450 °C under $N_2$ flow (50 mL/min).

**RESULTS AND DISCUSSION**

**I - Homogeneous nucleation model**

In order to reach a comprehensive description of the CaPs precipitation reaction pathways, a kinetic model of homogeneous nucleation was developed. This model was aimed at providing access to the nucleation rates of the different CaPs in order to identify the potential precursors of the thermodynamic products (DCPA or HAp)[28] depending on the synthesis parameters (pH, temperature and order of introduction of the precursors).

In a supersaturated solution, the precipitation process starts with the appearance of unstable germs that can evolve into stable nuclei when they are able to overcome an energy barrier $\Delta G$ (J) that allows them to reach a particular critical size.[30,31] In that respect, the homogeneous nucleation rate $J$ (germ/(m³·s)) can be expressed as:

$$J = J_0 \mathrm{e}^{\frac{-\Delta G}{k_B T}} \ (\text{Eq. 1})$$

where $k_B$ (J/K) is the Boltzmann constant, $T$ (K) is the temperature and $J_0$ a characteristic rate. For an ideal HAp material, $\Delta G^{HAp}$ corresponds to the minimum energy required for a germ to reach a critical size beyond which the corresponding nucleus grows to form a crystal $(Ca_5(PO_4)_3OH)_N$ with $N \gg 1$. According to this model, this energy barrier is expressed as:

$$\Delta G^{HAp} = \frac{f \omega^2 {\gamma_{SL}}^3}{k_B^2 T^2 (5 + 3 + 1)^2 (\ln S^{HAp})^2} \ (\text{Eq. 2})$$

Eq. 2 involves different parameters, namely a form factor $f$ $(= \frac{16\pi}{3}$ for spherical nuclei), the molecular volume $\omega$ (m$^{-3}$) of Ca$_5$(PO$_4$)$_3$OH, the nuclei/solvent surface tension $\gamma_{SL}$ (J/m$^3$) and the supersaturation ratio $S^{HAp}$. For an ionic solid such as HAp, $S^{HAp}$ is defined, at an out-of-equilibrium time $t$, according to the following equation:

$$S^{HAp} = \left( \frac{a(\text{Ca}^{2+})_t^5 a(\text{PO}_4^{3-})_t^3 a(\text{OH}^-)_t}{K_s^{HAp}} \right)^{\frac{1}{5+3+1}} \text{ (Eq. 3)}$$

where $a(i)_t = \gamma(i)_t \frac{c(i)_t}{c^\circ}$ is the ionic activity of $i$ at $t$ calculated from the concentration $c(i)_t$, the standard concentration $c^\circ$ of 1 mol/L and the activity coefficient $\gamma(i)_t$ determined *via* the Davies equation derived from the Debye-Hückel theory. $K_s^{HAp}$ is the solubility product of HAp. The supersaturation ratio $S$ for all CaPs is found to be pH-dependent because of the Brønsted basic properties of PO$_4^{3-}$ and OH$^-$ anions (Figure S3). As $K_s$ is a $T$-dependent parameter, $S$ should be also impacted by the temperature of the precipitation medium. The supersaturation ratios used for the others CaPs are detailed in the *Supporting Information* (*Homogeneous nucleation model*). Based on earlier literature data (Table 1), the nucleation kinetics of HAp, ACP, OCP and DCPD in water could be compared. The homogeneous nucleation energy barrier ($\Delta G$) was plotted as a function of the pH of the reaction medium at the very beginning of the Ca → P and P → Ca routes at 80 (Figure 1A) and 37 °C (Figure 2). This was carried out by considering the supersaturation ratio after the addition of the first drop of one precursor ion solution into the reactor containing the other precursor ion solution (section *Materials and Methods*). On this limited range of temperatures, it is found that this parameter does not have a significant influence on the homogeneous nucleation energy barrier. Hence, the precipitation pathways established at 37 °C (Figure 2) for the syntheses carried out at pH 4.2, 6.5 and 9.0, are found to be identical to those

established at 80 °C (Figure 1). At a given pH, the CaP that precipitates first is the one exhibiting the lowest energy barrier $\Delta G$. Figure 1A shows that the HAp nuclei never precipitate first, which indicates that this mineral must be formed from another CaP mineral. In an acidic to neutral medium, the formation of the OCP mineral $Ca_8(HPO_4)_2(PO_4)_4 \cdot 5H_2O$ is found to be kinetically favored at the beginning of both $Ca \rightarrow P$ and $P \rightarrow Ca$ routes (Figure 1A) while under alkaline conditions, ACP $(Ca_3(PO_4)_2)$ is the kinetically favored precipitated CaP material. This result is of particular interest as it provides further support on the fact that OCP should be the precursor of HAp under physiological conditions (pH 7.4 and 37 °C, Figure 2) as mentioned in numerous biomineralization studies.[32–36] The kinetically favored precipitation of OCP compared to that of ACP under slightly acidic conditions is partly related to the higher stability of OCP constitutive hydrogen phosphate anions $HPO_4^{2-}$ (not present in ACP) than phosphate anions $PO_4^{3-}$ ( *Supporting Information* Figure S3, Eqs. S1, S2). Figures 1A and 2 show that the change in the nature of the kinetic products (OCP/ACP) appears around pH 8.1–8.8 and 7.0–7.4 at the beginning of the $Ca \rightarrow P$ (Figures 1A**a**, 2**a**) and $P \rightarrow Ca$ (Figures 1A**b**, 2**b**) routes, respectively. Figure 1A shows that the nucleation of ACP is kinetically favored over that of OCP in a wider pH range for the $P \rightarrow Ca$ route compared to the $Ca \rightarrow P$ route. Such a difference may be partly attributed to the greater $Ca/P$ ratio of ACP $(Ca/P = 1.50)$ compared to that of OCP $(Ca/P = 1.33)$ and the improved associated nucleation rate in Ca-rich solutions. Depending on the nature of the calcium and phosphate precursors, the counterions may have an influence on the precipitation reaction pathways. Typically, if the counterions can lead to the formation of stable complexes (citrate anion, ethylenediaminetetraacetate anion $(EDTA^{4-})$, etc.), the proposed model should be adapted to consider the complexation equilibria that impact the speciation of the $Ca^{2+}$ and $PO_4^{3-}$ ions in solution and the growth of crystallites by complexation reactions on their surface. In contrast, if

the counterions ($NH_4^+$, $NO_3^-$, $Cl^-$, etc.) cannot lead to the formation of stable complexes in solution with calcium and/or phosphate species, their influence will be limited to changes in the ionic strength of the reaction medium and thus, to changes in the activity coefficients $\gamma(i)_t$ of the dissolved species. For reaction media exhibiting similar ionic strengths, a limited influence of the nature of the counterions can be expected on the CaPs precipitation reaction pathways. In most cases, including this study, the HAp is precipitated from precursors such as $H_3PO_4$, $NH_4H_2PO_4$, $Ca(NO_3)_2 \cdot 4H_2O$, $Ca(OH)_2$ and/or $CaCl_2$, which release rather inert counterions with regard to calcium and phosphate species in solution and on the surface of the precipitated particles. Consequently, the presence of such counterions in solution should not influence the CaPs precipitation reaction pathways to a significant extent.

**Table 1.** $\omega$ and $\gamma_{SL}$ data used for the modelling of the Homogeneous Nucleation Kinetics of the different CaPs (HAp, ACP, OCP and DCPD).[a]

| Nuclei | $\omega$ (m$^3$) | $\gamma_{SL}$ (J/m$^3$) | $K_s^{CaP}$(80 °C)[28] |
|---|---|---|---|
| **HAp**: $Ca_5(PO_4)_3OH$ | $2.63 \times 10^{-28}$ | 0.010* | $10^{-59.6}$ |
| **ACP**: $Ca_3(PO_4)_2$ | $1.40 \times 10^{-28}$ | 0.004* | $10^{-31}$ |
| **OCP**: $Ca_4(HPO_4)(PO_4)_2 \cdot \frac{5}{2}H_2O$ | $3.11 \times 10^{-28}$ | 0.004* | $10^{-49.5}$–$10^{-52.5}$ |
| **DCPD**: $Ca(HPO_4) \cdot 2H_2O$ | $1.27 \times 10^{-28}$ | 0.001* | $10^{-7}$ |
| **DCPA**: $Ca(HPO_4)$ | $3.90 \times 10^{-28}$ | – | $10^{-7.40}$ |

[a]For ACP, $\omega$ was approximated from the size of Posner's clusters (spheres of 9.5 Å diameter).[12] The HAp, OCP and DCPD surface tensions were taken from earlier studies,[35,37] whereas the one for ACP was approximated to that of β-$Ca_3(PO_4)_2$,[38] which exhibits a crystallographic structure close to that of ACP. *Large uncertainty on these values. The lack of quantitative data for the $\gamma_{SL}$ of DCPA does not allow it to be included in the kinetic model, although the absence of water in its crystalline structure compared to DCPD suggests that $\gamma_{SL}^{DCPA} > \gamma_{SL}^{DCPD}$ and therefore $\Delta G^{DCPA} > \Delta G^{DCPD}$ at a given pH (Eq. 2).
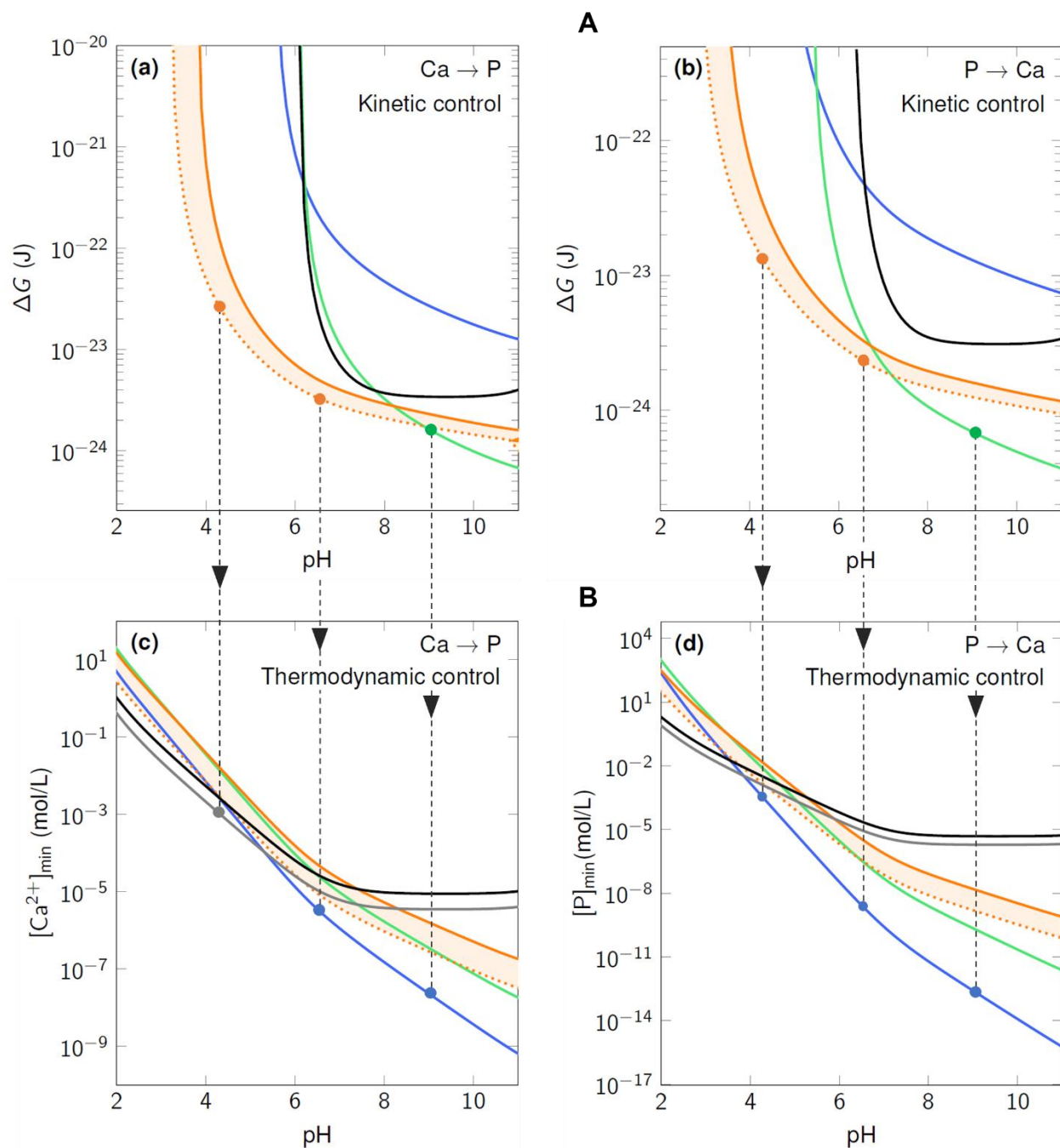
**Figure 1.** (**A**) Homogeneous nucleation energy barriers ($\Delta G$) calculated as a function of the pH at 80 °C and at the beginning of synthesis, *i.e.* when a drop of the calcium solution is introduced into a reactor containing the phosphate solution (**a**, Ca → P, $[P]_0 = 0.13$ mol/L) or *vice versa* (**b**, P → Ca, $[Ca^{2+}]_0 = 0.22$ mol/L) for CaPs. For OCP, an area is plotted due to the uncertainty in the value of its solubility product at 80 °C (Table 1). Note that below pH 3, no nucleation is expected when the first drop of solution is added as the condition $S > 1$ is not verified. (**B**) From kinetically

12

(**a** and **b**) to thermodynamically controlled (**c** and **d**)[28] synthesis of CaPs, predicted at the beginning of the addition step for the routes Ca → P (**a** and **c**) and P → Ca (**b** and **d**) at 80 °C. The vertical arrows represent the reaction precipitation pathways of CaPs at pH 4.2, 6.5 and 9.0. CaPs: HAp (blue), ACP (green), OCP (orange), DCPD (black) and DCPA (grey).
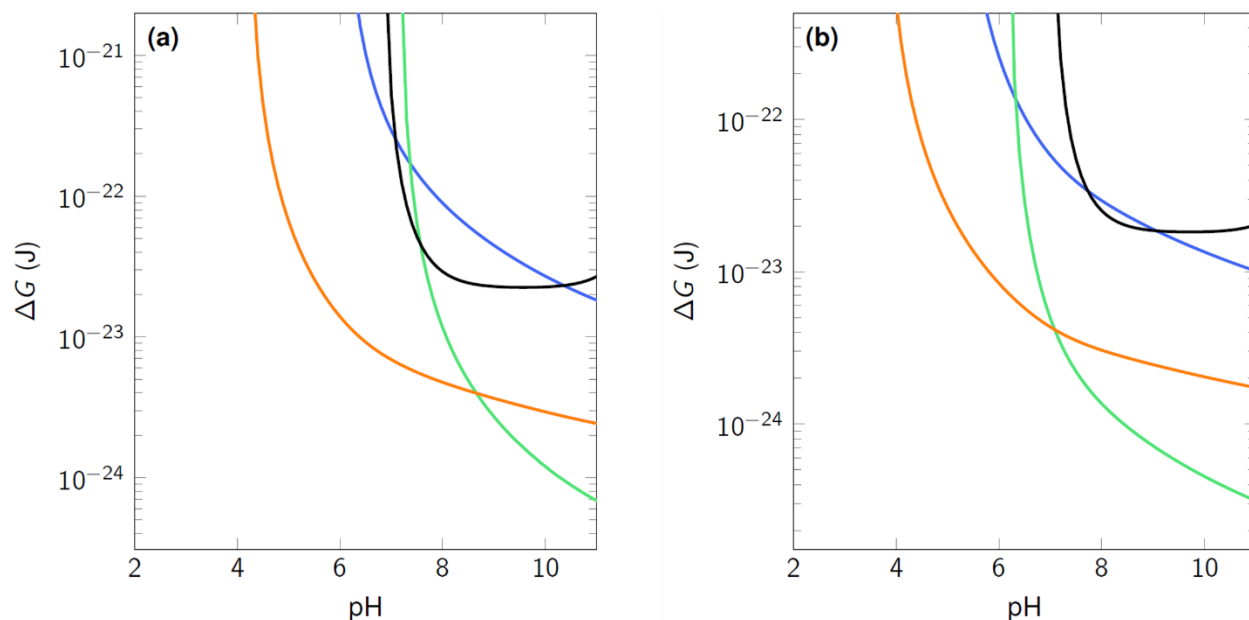


**Figure 2.** Homogeneous nucleation energy barriers $\Delta G$ calculated as a function of the pH of the reaction medium at 37 °C at the beginning of synthesis when a drop of the calcium solution is introduced into the reactor containing the phosphate solution (**a**, Ca → P, $[P]_0 = 0.13$ mol/L) or *vice versa* (**b**, P → Ca, $[Ca^{2+}]_0 = 0.22$ mol/L) for HAp, ACP, OCP and DCPD. Note that below pH 3–4, no nucleation is expected when the first drop is added as the condition $S > 1$ is not verified.

## II. Experimental Identification of the Reaction Intermediates in CaP Precipitation

### II - 1. *In Situ* Raman Monitoring

CaPs were synthesized using an automated reactor (Figure S1) allowing for the differentiation of two synthesis routes, Ca → P and P → Ca, involving the dropwise addition of a solution (containing $Ca^{2+}$ or $PO_4^{3-}$ ions) into a solution containing the other precursor ($PO_4^{3-}$ or $Ca^{2+}$ ions).

In order to probe the formation of OCP or ACP at the beginning of the syntheses, as predicted by the homogeneous nucleation model (section *I*), the CaP precipitation was monitored by *in situ* Raman spectroscopy (*Materials and Methods*). Materials formed transiently as a function of the time of reaction during the addition step (slow addition rate of 2.2 mL/min) were probed for the Ca → P route at pH 6.5 and 9.0 (Figure 1A**a**, samples 3 and 7, Table 2). First, from Figures 3 and S4 at 0 min, Raman bands associated with $H_2PO_4^-$ anions (at 879 and 1077 cm$^{-1}$) and $HPO_4^{2-}$ anions (at 985 cm$^{-1}$) are observed. The higher relative intensities of the two former bands at pH 6.5 compared to those at pH 9.0 are fully consistent with the speciation of the phosphate species in the initial solutions at a given pH value (higher concentration of $H_2PO_4^-$ ions at pH 6.5 than at 9.0). Although the intensities of these contributions associated with hydrogen phosphate species $H_xPO_4^{(3-x)-}$ in solution progressively decreases as the time of addition of the calcium solution increases, two sets of new contributions are observed: that at 1050 cm$^{-1}$ is due to nitrate anions[39] progressively introduced in the reactor and that in the 949–966 cm$^{-1}$ range is ascribed to the phosphate groups in the precipitated particles (Figure S4). At pH 6.5 (Figure 3**a**), the two characteristic contributions of the OCP phase (at about 959 and 966 cm$^{-1}$, Table S2) appear within the first 10 min of addition of the calcium solution. From 20 min, the shoulder at 966 cm$^{-1}$ becomes less and less defined and the maximum of the main contribution progressively shifts to 960 cm$^{-1}$ over time. Such an evolution indicates that OCP progressively transforms into HAp.[40] These *in situ* Raman data indicate rather the formation of the thermodynamically most stable HAp phase under these conditions *via* an OCP phase precursor. The OCP → HAp transformation will be discussed in detail in section *III*. The evolution of the Raman contributions shown in Figure 3**a** for the synthesis carried out at pH 6.5 *via* the Ca → P route is therefore fully consistent with the earlier thermodynamic[28] (Figure 1B**c**) and present kinetic predictions (Figure 1A**a**).

At pH 9.0, the Raman spectra collected during the precipitation step are not as conclusive as those recorded for the experiment monitored at pH 6.5. During the first 20 min of the reaction, neither ACP nor OCP precursor of HAp could be identified as the Raman contribution characteristic of HAp, around 960 cm$^{-1}$, appeared as early as after 15 min of addition (Figure 3**b**). Note that the ACP phase has already been observed by *in situ* Raman spectroscopy as the HAp precursor in alkaline medium by Stammeier *et al.* during a synthesis carried out at 20 °C and pH 9.2 following the Ca → P route with an addition rate of 5 mL/min.[41] The difficulty in observing the ACP amorphous phase transiently in the present study may be attributed, at least in part, to the insufficient concentration of ACP particles at the beginning of the addition phase due to the too rapid transformation of ACP to HAp at 80 °C. To overcome such issues that prevent the determination of the chemical pathways toward the thermodynamic compounds under these operating conditions (samples 3 and 7, Table 2), new syntheses have been carried out under conditions likely to favor a kinetic control.
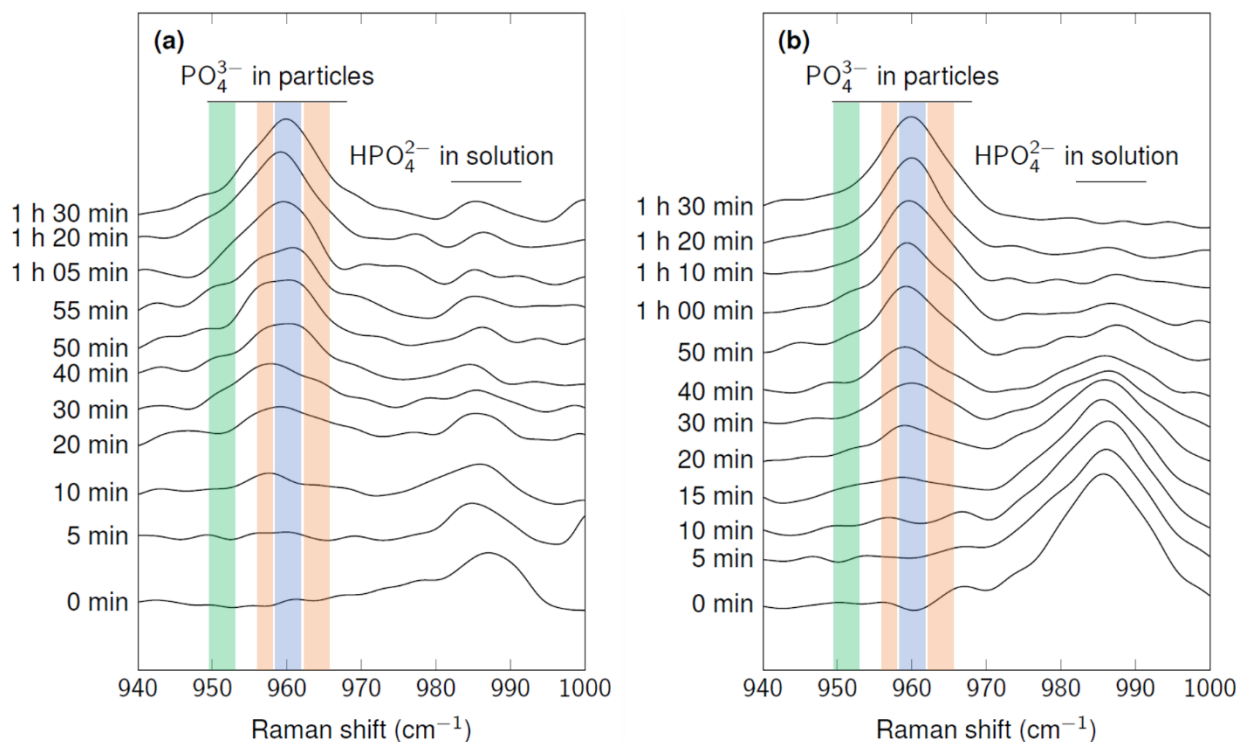
**Figure 3.** *In situ* monitoring of the precipitation of CaPs by Raman spectroscopy during the addition step of syntheses carried out at pH 6.5 (**a**) and 9.0 (**b**) following the Ca → P route at 80 °C with an addition rate of 2.2 mL/min. The colored areas correspond to the Raman shift domains associated with the vibration mode $v_1(PO_4)$ of HAp (blue), ACP (green) and OCP (orange). The spectra at time 0 min are those recorded for the reaction media initially containing only the phosphate solution of initial concentration $[P]_0 = 0.13$ mol/L at pH 6.5 (**a**) and 9.0 (**b**). Figure 3 is a zoomed image of the 940–1000 cm$^{-1}$ absorption area of the spectra reported in Figure S4.

## II - 2. Synthesis under Kinetic Control

In a previous study, thermodynamically-controlled syntheses carried out at pH 9.0 or 6.5 were found to lead to the formation of HAp materials (samples 2–8, Table 2), whereas DCPA was obtained following the Ca → P route at pH 4.2 (sample 12, Table 2).[28] New syntheses were carried out at pH 9.0, 6.5 and 4.2, under conditions likely to favor the formation of kinetically controlled

16

materials (sample A–G, Table 2), so as to isolate metastable CaP phases different from the thermodynamic products. The addition rate of one precursor solution to the other appeared to be an easy-to-handle operating parameter for the preferential formation of the thermodynamically (slow addition rate of the precursor solution) or kinetically controlled (fast addition rate of the precursor solution) CaPs. The high initial precursor concentrations ($[Ca^{2+}]_0 = 0.22$ mol/L and $[P]_0 = 0.13$ mol/L) and the targeted final ratio $[Ca^{2+}]/[P]$ (set to 1.67, unless otherwise specified, Table 2) were selected in order to be able to correlate the results from the present study to those of our earlier work.[28] Under these conditions, CaPs of different nature are obtained depending on the pH of the reaction medium, the reaction temperature and/or the synthesis route used (samples A–G, Table 2).

Under basic conditions at pH 9.0 and 37 °C, a crystalline material is obtained with all diffraction lines attributable to the HAp structure for the P → Ca route (sample A, Figure 4a). The absence of OCP is further supported by the-low angle diffraction pattern (Figure S5a) and Raman spectroscopy (Figure 5a). In agreement with these XRD data, the Ca/P ratio of 1.59 determined for sample A (Table 2) and the presence of $HPO_4^{2-}$ defects revealed by Raman spectroscopy (contributions at 870–920 and 1000–1015 cm$^{-1}$, Figure 5a, Table S2) corroborate the formation of a calcium-deficient HAp under these conditions. Table 2 shows that a decrease in the temperature from 80 (sample 2) to 37 °C (sample A) and an increase in the addition rate of the phosphate solution from 2.2 (sample 2) to 50 mL/min (sample A) did not allow isolation of the ACP kinetic product in sample A, as however expected from the homogenous nucleation model (Figure 1A**b**). Although *in situ* Raman spectroscopy could not provide any evidence for the intermediate formation of ACP in the synthesis carried out at pH 9.0, 80 °C and *via* the Ca → P route (Figure 3**b**, sample 3), the synthesis performed under kinetically controlled conditions (Ca →

P route, 37 °C and 50 mL/min addition rate, sample B, Table 2), led to the formation of an amorphous material showing no long-range order (sample B, Figure 4**a**). The Ca/P ratio of 1.52 of sample B (Table 2) is consistent with that of an ACP phase that likely contains mainly $Ca_9(PO_4)_6$ clusters.[12,42] The Raman spectrum of sample B was found to be comparable to that of sample A (Figure 5**a**), albeit the Raman contributions of sample B appeared to be slightly broader compared to those of sample A. The presence of $HPO_4^{2-}$ contributions in sample B at 870–920 and 1000–1015 cm$^{-1}$ (Table S2) and the shift in the $\nu_1(PO_4)$ band to higher Raman shifts (964 cm$^{-1}$) than that expected for ACP (Table S2) may be attributed to a moderate transformation of ACP to HAp. Such a result is expected in view of the ACP → HAp mineralization pathway predicted at pH 9.0 using the kinetic precipitation model developed in the present work (Figure 1A). Given that HAp has been shown to be the most stable thermodynamic CaP at pH 9.0 (Figure 1B),[28] the formations of HAp in sample A and mainly of ACP in sample B indicate that the transformation of ACP to HAp is kinetically favored by the P → Ca route.

At pH 6.5 and at 80 °C, the increase in the addition rate of the phosphate solution in the P → Ca route (sample 5 *vs* sample C) does not impact the nature of the CaP formed. As observed by XRD (Figure 4**b**) and Raman spectroscopy ($\nu_1(PO_4)$ band centred at 962 cm$^{-1}$, Figure 5**b**), HAp was obtained for sample C. This suggests that kinetic control of the precipitation reaction is difficult to achieve for the P → Ca route by only modifying the addition rate of the phosphate solution at pH 6.5 and 80 °C. It can be noted, however, that the nucleation, growth and phase transformation of the particles are modified, as illustrated in the increase of the specific surface area from 15 to 54 m$^2$/g and the decrease in the Ca/P ratio from 1.63 to 1.61 for samples 5 and C, respectively (Table 2). In contrast, at the end of the syntheses at pH 6.5 following the Ca → P route at 37 or 80 °C with an addition rate of 2.2 or 50 mL/min (sample D or sample E), the final Ca/P = 1.37 or

1.34 molar ratio may indicate the presence of OCP with or without another CaP phase. The presence of OCP in sample D and E is supported by both low and high-angle XRD (Figures 4**b** and S5**b**), and the characteristic Raman $\nu_1(PO_4)$ vibration modes at 959 and 966 cm$^{-1}$ (Figure 5**b**, Table S2). The fact that the resolution of the Raman bands at 959 and 966 cm$^{-1}$ decreases for sample D compared to sample E (Figure 5**b**) together with a slight increase in the Ca/P ratio in sample D (1.37) compared to sample E (1.34) suggests the presence of traces of HAp in sample D. To summarize, at pH 6.5, (*i*) HAp was only produced in the thermodynamically-controlled synthesis of sample 7 (80 °C and 2.2 mL/min addition rate), (*ii*) HAp was only present as traces with OCP in sample D (37 °C and 2.2 mL/min addition rate) and (*iii*) pure OCP was formed in sample E (80 °C and 50 mL/min addition rate). These data suggest that kinetic control of CaP precipitation *via* the Ca → P route is more easily achieved by increasing the addition rate of the calcium solution (in the 2.2–50 mL/min range) rather than by decreasing the reaction temperature (in the 37–80 °C range). In addition, comparison of sample C (P → Ca route, pH 6.5, 80 °C and 50 mL/min addition rate, pure HAp phase) and sample D (Ca → P route, pH 6.5, 80 °C and 50 mL/min addition rate, mixture of OCP and HAp) indicates that the transformation of OCP to HAp is kinetically favored by the P → Ca route. Hence the order of introduction of the precursors also appears to be a key synthesis parameter of the CaPs.

In a more acidic medium (pH 4.2), the OCP material is formed together with other CaPs depending on the synthesis route (samples F and G). High-angle XRD (Figure 4**c**) shows the presence of OCP, DCPD and DCPA crystalline phases in sample G that was prepared *via* the Ca → P route. DCPD and DCPA also exhibit a characteristic Raman contribution at *ca.* 986 cm$^{-1}$ (Figure 5**c**) assigned to their $\nu_1(HPO_4)$ vibrational mode (Table S2). The resulting average Ca/P ratio of 1.31 measured for this multiphasic sample lies consistently between those of OCP (Ca/P = 1.33)

and DCPD/DCPA (Ca/P = 1.00). Regarding the P → Ca route (sample F), the average Ca/P ratio of 1.42 is found to be consistent with the presence of OCP and HAp, as shown on its high-angle XRD pattern (Figure 4**c**) and by the shift of the maximum of the $v_1(PO_4)$ Raman band to 961 cm$^{-1}$ (Figure 5**c**). The absence of Raman contribution at 986 cm$^{-1}$ in sample F (Figure 5**c**) indicates that DCPD and DCPA were not formed in this sample. It must be recalled that the HAp and DCPA phases have been predicted to be the most stable thermodynamic phases at the beginning of the syntheses carried out at pH 4.2 *via* the P → Ca and Ca → P routes, respectively (Figure 1B).[28] The presence of an additional OCP phase therefore indicates that the corresponding syntheses carried out at pH 4.2 were at least, partially kinetically controlled in the present work in agreement with the prediction of the homogeneous nucleation model (Figure 1A). The presence of the DCPD phase in the case of the Ca → P route (sample G in Table 2) also suggests the formation of another intermediate to the DCPA, as discussed in the next section.
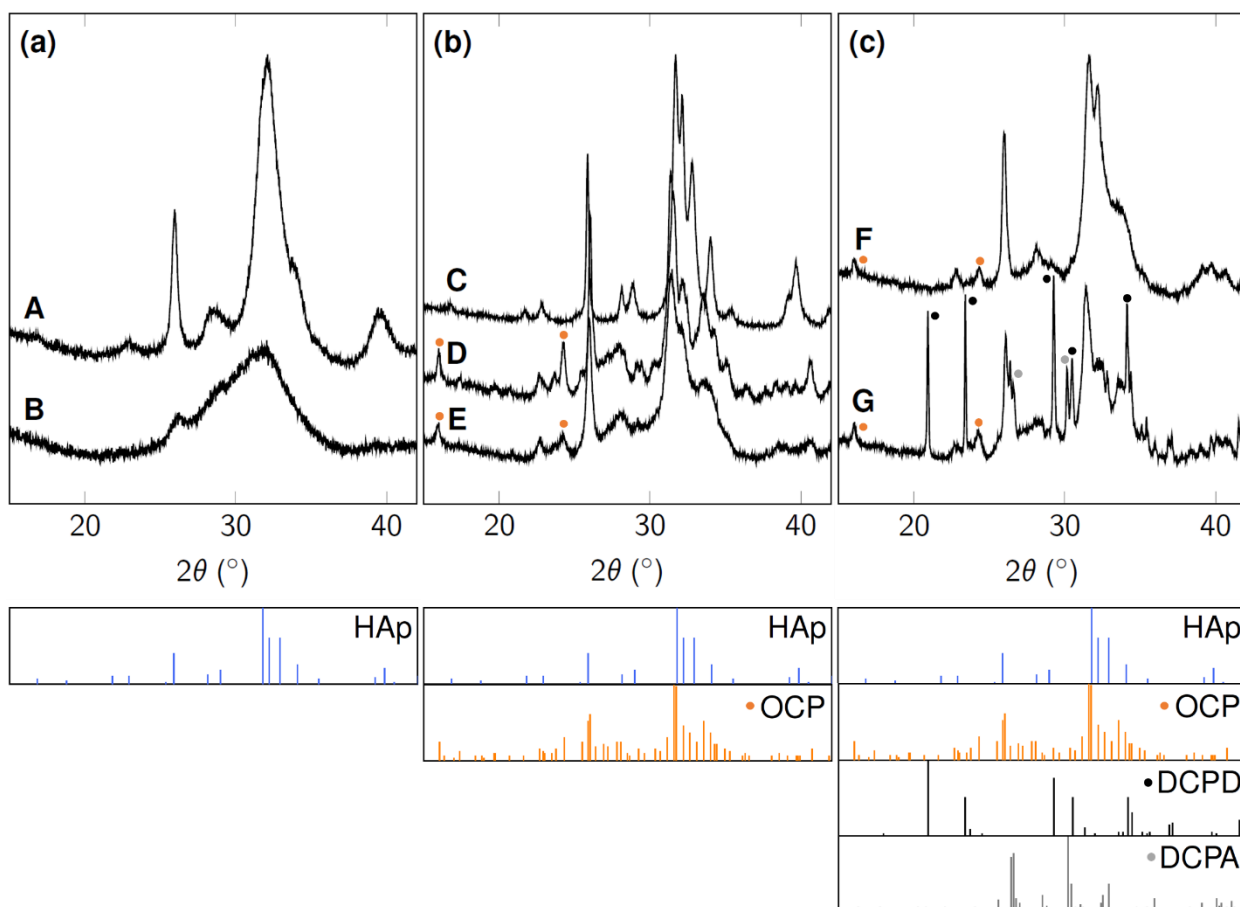
**Figure 4.** Diffraction patterns of samples A and B prepared at pH 9.0 (**a**), C, D and E prepared at pH 6.5 (**b**), and F and G prepared at pH 4.2 (**c**). The position of the diffraction lines for the different CaPs is highlighted by coloured bars: HAp (blue, ICDD reference card n° 00-009-0432), OCP (orange, ICDD reference card n° 00-026-1056), DCPA (grey, ICDD reference card n° 00-009-0080), DCPD (black, ICDD reference card n° 00-009-0077). The ●, ● and ● symbols indicate the discriminant lines in high-angles diffraction patterns for the OCP, DCPD and DCPA phases, respectively. At pH 9.0 (**a**), 6.5 (**b**) and 4.2 (**c**), the HAp/ACP, HAp/OCP and HAp/OCP/DCPD(A) phases were obtained, respectively.
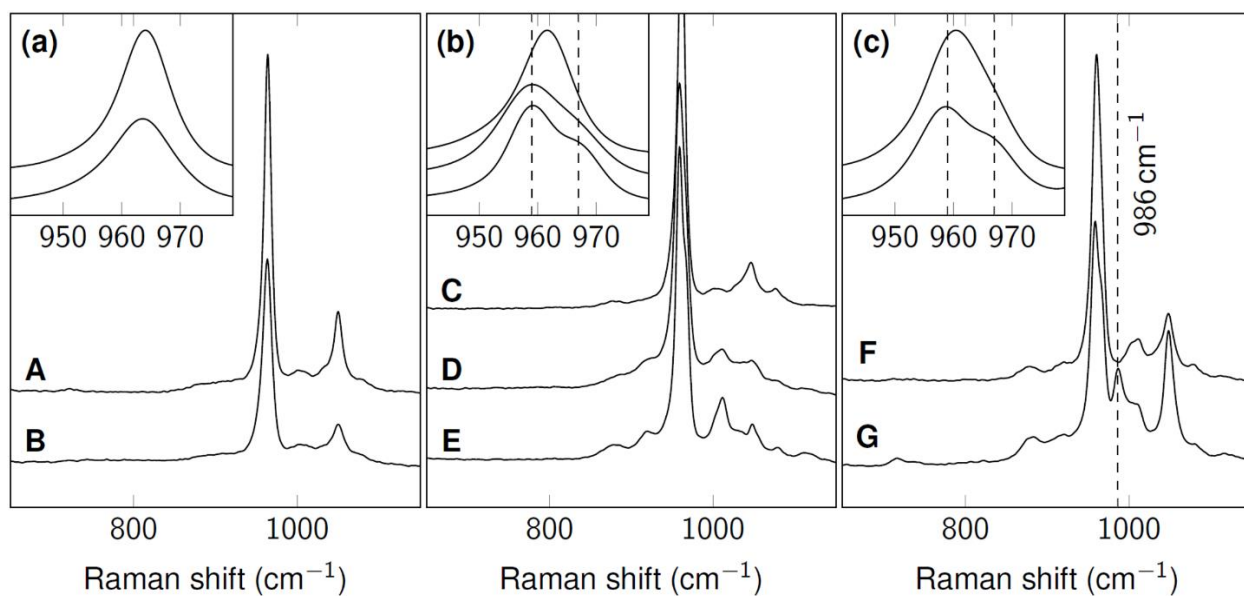
**Figure 5.** Raman spectra and associated magnification between 940 and 980 cm$^{-1}$ for samples A and B prepared at pH 9.0 (**a**), C, D and E prepared at pH 6.5 (**b**) and F and G prepared at pH 4.2 (**c**). The characteristic elongation modes $\nu_1(PO_4)$ for OCP at 959 and 966 cm$^{-1}$ are indicated by dashed lines as well as the position of the elongation mode $\nu_1(HPO_4)$ for DCPD at 986 cm$^{-1}$ (Table S2).

**Table 2.** Description of the Experimental Conditions Applied in the Synthesis of Calcium Phosphates to Favor Either a Thermodynamic or a Kinetic Control, Crystalline Phases Identified by XRD, Ca/P Molar Ratios Determined by XRF and Specific Surface Areas (SSA) of the Synthesized Materials.

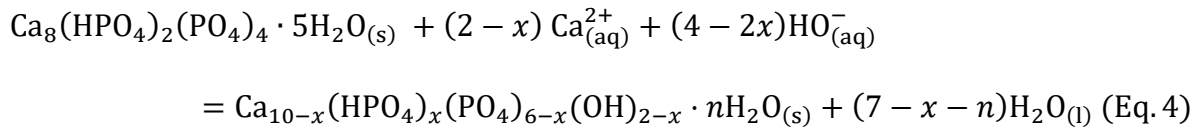| Sample reference | pH | Synthesis route | T (°C) | Targeted $[Ca^{2+}]/[P]$ | Addition rate (mL/min) | Phase(s) | Ca/P | SSA ($m^2$/g) |
|---|---|---|---|---|---|---|---|---|
| **Syntheses whose parameters have been chosen to favor a thermodynamic control[28]** | | | | | | | | |
| 2[a] | | P → Ca | 80 | 1.67 | 2.2 | HAp | 1.72 | 38 |
| 3[a] | 9.0 | | 80 | 1.67 | 2.2 | HAp | 1.66 | 102 |
| 4[a,b] | | Ca → P | 37 | 1.67 | 2.2 | HAp | 1.65 | 195 |
| 5[a] | | P → Ca | 80 | 1.67 | 2.2 | HAp | 1.63 | 15 |
| 6[a] | 6.5 | | 37 | 1.67 | 2.2 | HAp | 1.52 | 122 |
| 7[a] | | Ca → P | 80 | 1.67 | 2.2 | HAp | 1.53 | 44 |
| 8[a] | | | 80 | 1.50 | 2.2 | HAp | 1.53 | 43 |
| 12[a] | 4.2 | Ca → P | 80 | 1.67 | 2.2 | DCPA | 1.04 | < 2 |
| **Syntheses whose parameters have been chosen to favor a kinetic control** [This study] | | | | | | | | |
| A | 9.0 | P → Ca | 37 | 1.67 | 50 | HAp | 1.59 | 165 |
| B | | Ca → P | 37 | 1.67 | 50 | ACP + HAp | 1.52 | 78 |
| C | | P → Ca | 80 | 1.67 | 50 | HAp | 1.61 | 54 |
| D | 6.5 | | 37 | 1.67 | 2.2 | OCP + HAp | 1.37 | 63 |
| E | | Ca → P | 80 | 1.67 | 50 | OCP | 1.34 | 37 |
| F | | P → Ca | 80 | 1.67 | 50 | OCP + HAp | 1.42 | 75 |
| G | 4.2 | Ca → P | 80 | 1.67 | 50 | OCP + DCPD(A) | 1.31 | 33 |

[a] The references of the samples of interest are those used in the associated publication.

[b] At the end of the addition phase, the sample was aged for 2 h at the pH and temperature *T* of precipitation.

### III. Kinetic *Versus* Thermodynamic Control: toward the Establishment of Precipitation Reaction Pathways

The experimental observation of OCP in most of the syntheses carried out at pH 4.2 and 6.5 (samples D–G, Table 2), and at the beginning of the synthesis followed by *in situ* Raman spectroscopy at pH 6.5 (Figure 3**a**) is consistent with the predictions of the proposed kinetic model of nucleation in this pH domain (Figures 1 and 2). In particular, the precipitation reaction pathway OCP → HAp, proceeds *via* a hydrolysis reaction as described in Eq. 4 (with $x \leq 2$):

$$Ca_8(HPO_4)_2(PO_4)_4 \cdot 5H_2O_{(s)} + (2 - x)\,Ca^{2+}_{(aq)} + (4 - 2x)HO^-_{(aq)}$$

$$= Ca_{10-x}(HPO_4)_x(PO_4)_{6-x}(OH)_{2-x} \cdot nH_2O_{(s)} + (7 - x - n)H_2O_{(l)} \ (Eq. 4)$$

The occurrence of complete (sample C), partial (samples D, F and G) or delayed hydrolysis (sample E) of OCP is ascribed to the influence of operating parameters on the kinetics of this hydrolysis reaction, as discussed below.

At pH 4.2 and following the Ca → P route, the presence of a second intermediate, DCPD in sample G can be explained on the basis of the predicted hydration/dehydration pathway OCP → DCPD → DCPA (Figure 1) with the following equations:

$$Ca_8(HPO_4)_2(PO_4)_4 \cdot 5H_2O_{(s)} + 11H_2O_{(l)}$$

$$= Ca_6(HPO_4)_6 \cdot 12H_2O_{(s)} + 2\,Ca^{2+}_{(aq)} + 4HO^-_{(aq)} \ (Eq. 5)$$

$$Ca_6(HPO_4)_6 \cdot 12H_2O_{(s)} = Ca_6(HPO_4)_{6(s)} + 12H_2O_{(l)} \ (Eq. 6)$$
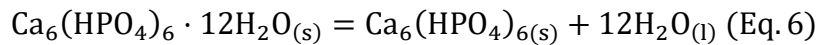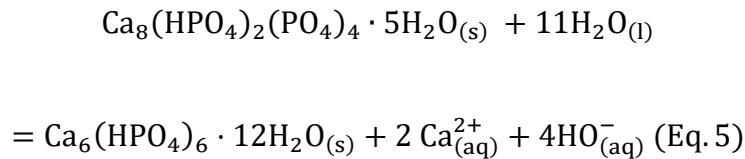
In an alkaline medium, the present kinetic nucleation model (Figures 1 and 2) predicts that ACP should precipitate first, whereas the thermodynamic model proposed earlier[28] indicates that HAp is the most stable CaP under these conditions. The ACP to HAp transformation proceeds *via* the hydrolysis reaction described using Eq. 7 (with $x \leq 1$):

$$Ca_9(PO_4)_6 + (1 - x) Ca^{2+}_{(aq)} + (2 - 2x)HO^-_{(aq)}$$

$$= Ca_{10-x}(HPO_4)_x(PO_4)_{6-x}(OH)_{2-x} \cdot nH_2O_{(s)} + (x - n)H_2O_{(l)} \text{ (Eq. 7)}$$
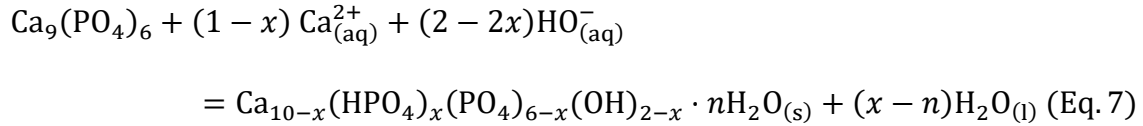
In agreement with these predictions, ACP was observed in sample B (Ca → P route, pH 9.0, and addition rate 50 mL/min, Table 2) prepared under kinetic control, whereas HAp was observed in sample 3 prepared under thermodynamic control (Ca → P route, pH 9.0, and addition rate 2.2 mL/min, Table 2), which validates the alkaline reaction pathway ACP → HAp for the Ca → P route (Figure 1). In the P → Ca route, the ACP material could not be observed, as HAp was only present in sample A (Table 2). As already mentioned for acidic pH, it is more difficult to achieve synthesis under kinetic control when following the P → Ca route compared to the Ca → P route (section *II - 2*). Such an influence of the order of introduction of the precursor is ascribed to the common ion effect. Equations 4 and 7 show that the conversion of OCP and ACP to HAp will be kinetically favored in a solution exhibiting an excess of calcium (P → Ca route) at a constant pH.[43,44] In contrast, an excess of phosphate ions (Ca → P route) does not influence the kinetics of these hydrolysis reactions, making the identification of the CaP intermediates involved in the formation of the HAp thermodynamic product much easier.

The determined precipitation pathways of CaPs illustrate the importance of the pH as a key parameter in controlling the supersaturation ratio (Eq. 3). The identification of the precipitation

pathways is the first step toward explaining the textural and structural differences observed for the synthesized of HAps depending on the P → Ca and Ca → P routes and the precipitation pH.[28]

## IV. Impact of the Chemical Pathways on the Properties of the Final HAp Samples

The previous sections have highlighted the different precipitation pathways leading to the formation of HAp. To discuss the influence of these precipitation pathways on the textural properties and composition of the prepared HAps, while avoiding any bias inherent to the multiphasic composition of most of the samples prepared under kinetically controlled conditions, this section focuses on HAp single-phase samples prepared under thermodynamic control (Table 2, samples 2 to 8).

### IV - 1. Influence of the Common Ion Effect on HAp Morphology

A wide variety of morphologies has been reported in the earlier literature for HAps synthesized under conditions[45–49] close to those used in our previous study.[28] To the best of our knowledge, rationalization of the influence of the synthesis parameters on the textural properties of HAps has been hardly reported to date, however, except for the reactant addition rate[46] (*Critical analysis of earlier literature studies* in *Supporting Information*). As shown previously,[28] the thermodynamically-controlled syntheses carried out at pH 6.5 and 9.0 led to the formation of HAp crystallites with various morphologies (platelets, hexagonal rods and needles recalled in Figure 6) and SSA ranging from 195 to 15 $m^2$/g (Table 2). Surprisingly, it was found that the order of introduction of the precursor ions into the reactor was a key parameter in controlling the textural properties of the HAp materials (sample 2 *vs* sample 3 obtained at pH 9.0 and sample 5 *vs* sample 8 obtained at pH 6.5, Table 2, Figure 6). This result suggests a strong influence of the common ion effect on the kinetics of hydrolysis of the ACP and OCP precursors to HAp (section *III*). In

other words, the nature of the initial solution, either rich in calcium (P → Ca) or phosphate (Ca → P) ions, in which the first nuclei are formed may be determinant for the HAp morphology. From earlier literature reports, the hydrolysis of OCP to HAp does not appear to involve a dissolution-reprecipitation process but rather a so-called *in situ*,[50–52] solid-solid,[53,54] topotactic[55–57] or solid-state[33,52] transformation due to the close crystallographic structure between both phases. In the P → Ca synthesis route carried out at pH 6.5 (sample 5), once the OCP nuclei were formed at the beginning of the addition step, their growth in crystallites with a platelet morphology (monoclinic space group of OCP) was inhibited due to their rapid solid-solid hydrolysis to HAp (Eq. 4). Hence, under these conditions, the HAp particles (hexagonal space group) were found to grow as hexagonal rods (Figure 6**a**).[28] By changing the order of introduction of the precursors, thus introducing the $Ca^{2+}$ ions in the phosphate solution (sample 8), the hydrolysis of the OCP nuclei should be kinetically limited in an initially phosphate-rich and calcium-poor solution. As a result, hydrolysis of OCP to HAp is delayed and occurs on particles that have already grown as platelets. In agreement with the earlier study of Terpstra and Bennema,[58] the observation of HAp nanoparticles exhibiting an elongated platelet morphology for sample 8 (Ca → P route), which is rather unexpected from the hexagonal space group symmetry of HAp, should result from the solid-solid transformation of OCP to HAp with the preservation of the OCP platelet morphology as illustrated in Figure 6**b**. In the syntheses carried out at pH 9.0, comparable explanations, albeit applying to ACP as the HAp intermediate (Figure 1), account for the formation of hexagonal HAp rods by the P → Ca route (sample 2, Figure 6**c**) and HAp needles of poorly-defined shape by the Ca → P route (sample 3, Figure 6**d**).

The higher length of the HAp rods obtained in the synthesis carried out at pH 6.5 compared to that carried out at pH 9.0 (sample 5 *vs* sample 2, Figure 6**a, c**) likely results from a competition

between nucleation and growth processes. Figure S3 shows that the supersaturation ratio is much higher for basic reaction media than for acidic ones for all of the CaPs. This obviously leads to a higher nucleation rate (Eq. 1) in the syntheses performed at pH 9.0 compared to those performed at pH 6.5, which is consistent with the formation of smaller crystallites in sample 2 (Figure 6**c**, pH 9.0) compared to those obtained for sample 5 (Figure 6**a**, pH 6.5).

All of these differences in morphology and crystallite sizes for the synthesized HAp materials went along with differences in SSA of 15 to 38 $m^2$/g for the hexagonal rods (samples 5 and 2), 43 $m^2$/g for the platelets (sample 8) and 102 $m^2$/g for the needles (sample 3). These synthesis conditions-morphology relationships appear to be valid to rationalize the data obtained in earlier studies, in which the authors observed structural and textural modifications of HAp by modulating synthesis parameters such as the pH, the addition rate or the order of introduction of the precursor ions (*Critical analysis of earlier literature studies* in *Supporting Information*).[45–49] This accounts for the robustness of the proposed models. The preparation of HAps exhibiting high SSA is of prime importance for their use as heterogeneous catalysts and depolluting agents. According to the set of syntheses performed to date under thermodynamic control (Table 2),[28] it appears that the preparation of HAps with large surfaces is promoted by the use of a high pH (sample 3 *vs* sample 7), a Ca → P route (sample 3 *vs* sample 2) and a low temperature (sample 4 *vs* sample 3 and sample 6 *vs* sample 5). Based on the proposed precipitation pathways (Figures 1 and 6**d**), all of these experimental parameters are in favor of the intermediate formation of ACP that should be slowly hydrolyzed to HAp during the addition step.
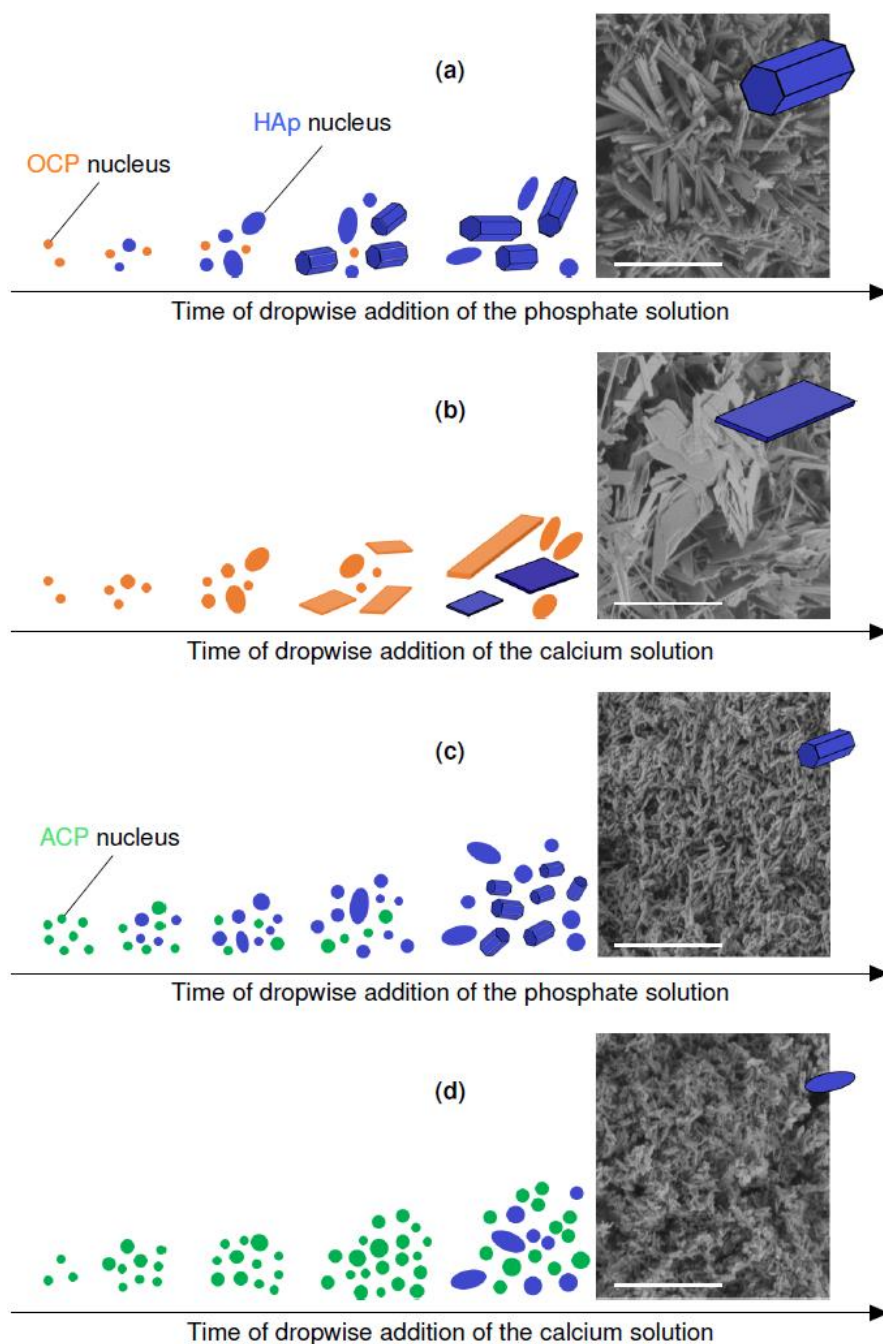
**Figure 6.** Schematic representation of the precipitation of HAp by nucleation, growth and solid-solid transformation at the origin of the morphologies observed for samples 5 (**a**) and 8 (**b**) prepared at pH 6.5 following the P → Ca and Ca → P routes, respectively, and for samples 2 (**c**) and 3 (**d**) prepared at pH 9.0 following the P → Ca and Ca → P routes, respectively. These HAp samples are those produced in the thermodynamically-controlled syntheses (Table 2). The scale bar on the SEM micrographs extracted from our earlier study:[28] 2 µm.

**IV - 2. Modulation of the Ca/P Ratio: Crystal Defects in the >Hydroxyapatite Structure**

**Hydrogen Phosphate Defects.** The HAp lattice is known to be quite flexible, which can therefore lead to the accommodation of crystal defects such as impurities or vacancies. In particular, the presence of hydrogen phosphate groups leads to the formation of under-stoichiometric materials with the following formula: $Ca_{10-x}(HPO_4)_x(PO_4)_{6-x}(OH)_{2-x} \cdot nH_2O$ ($x = 0\text{–}1$ and $Ca/P = 1.67\text{–}1.50$). This under-stoichiometry is attributed to a calcium deficiency in HAps,[59] which can be quantified by XRF based on the $Ca/P$ ratio (section *Materials and Methods*). Except sample 2, in which the $Ca/P$ ratio appears to be over-stoichiometric, all of the HAp samples are found to be more or less under-stoichiometric (samples 3–8, Table 2, $Ca/P <$ 1.67). As expected, this calcium deficiency is found to be associated with the presence of $HPO_4^{2-}$ defects identified by the Raman contributions at 879, 920 and 1011 cm$^{-1}$ assigned to the [P—OH] and $\nu_1(HPO_4)$ stretching modes (Figure 7**a**, Table S2). Figure 7**a** also shows that the intensity of the $HPO_4^{2-}$ Raman contributions increases as the $Ca/P$ ratio decreases. These observations thus indicate that the use of slightly acidic conditions is more favorable to the incorporation of $HPO_4^{2-}$ defects compared to the basic ones. This trend can be explained by the precipitation pathways proposed in the present study (Figures 1 and 6). In the syntheses carried out at pH 9.0, the HAp particles are formed from the solid-solid transformation of ACP[60,61] whose $Ca_9(PO_4)_6$ clusters do not contain any $HPO_4^{2-}$ groups. In contrast, in the syntheses carried out at pH 6.5, the HAp particles should be formed *via* the hydrolysis of an OCP intermediate exhibiting $HPO_4^{2-}$ entities in its crystalline structure. It is assumed that the partial hydrolysis of OCP (Eq. 4) would be responsible for the accommodation of such $HPO_4^{2-}$ defects in the apatite structure. Differences in $HPO_4^{2-}$ incorporation in the HAp materials, for which intermediate formation of OCP occurs depending on the synthesis route used at pH 6.5 and 80 °C, can also be accounted for from the

precipitation pathways. The greater incorporation of $HPO_4^{2-}$ entities in the HAp materials synthesized *via* the Ca → P route compared to those prepared by the P → Ca route (sample 7 *vs* sample 5 at pH 6.5, and Figure 7) can be attributed to the hydrolysis rate of the OCP reaction intermediate into HAp. As this rate is promoted by the presence of excess $Ca^{2+}$ ions in solution (Eq. 4), the P → Ca route is expected to lead to a more complete hydrolysis of the OCP intermediate at the end of the addition step compared to the Ca → P route, as the duration of the addition steps were identical in both syntheses. Overall, the incorporation of hydrogen phosphate defects in the apatite structure is favored by a decrease in the pH of the reaction medium (sample 2 *vs* sample 5 and sample 4 *vs* sample 7), a Ca → P synthesis route (sample 7 *vs* sample 5 and sample 3 *vs* sample 2) and a low temperature (sample 6 *vs* sample 5). Based on the proposed precipitation pathways (Figure 1), these parameters are likely to favor of the intermediate formation of OCP that slowly hydrolyzes to HAp during the addition step.
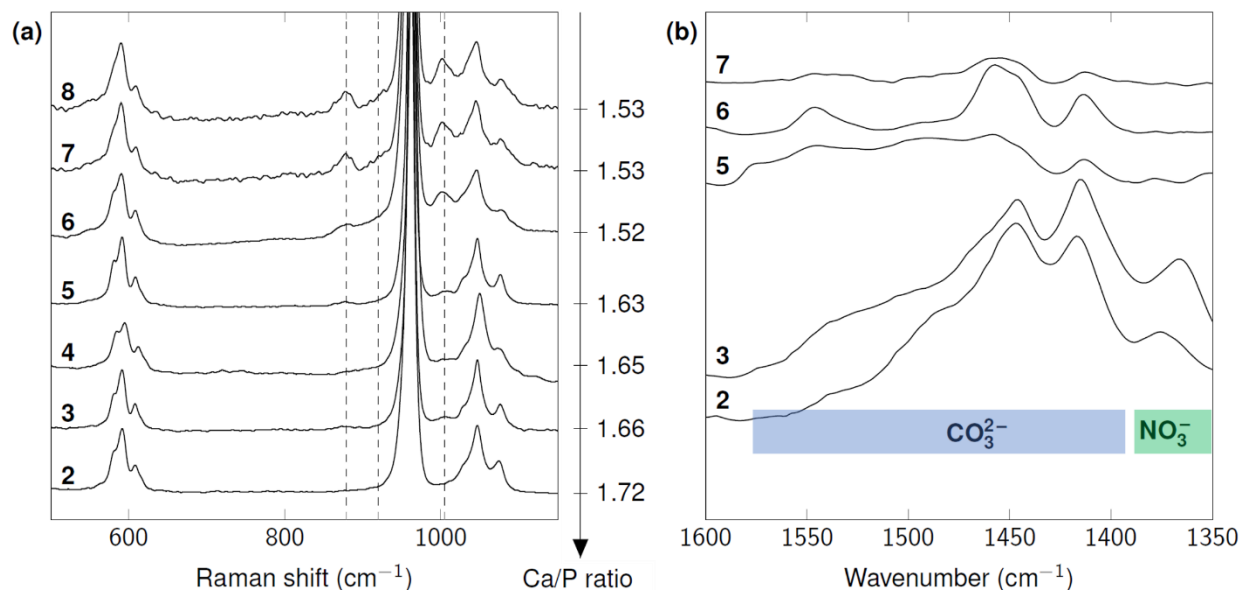


**Figure 7.** Raman spectra of HAp samples 2–8 (Table 2) normalized with respect to the $v_1(PO_4)$ band at *ca.* 962 cm$^{-1}$ and associated Ca/P ratios obtained by XRF (**a**). The Raman shifts of interest at 879, 920 and 1011 cm$^{-1}$, assigned to [P—OH] and $v_1(HPO_4)$ stretching modes of $HPO_4^{2-}$

31

groups (Table S2), are highlighted by vertical dashed lines. DRIFT spectra of HAp samples 2 and 3 prepared at pH 9.0 and 5–7 prepared at pH 6.5 acquired at 150 °C after an *in situ* pretreatment at 450 °C under flowing $N_2$ and normalized with respect to the phosphate combination bands around 2050 cm$^{-1}$ (**b**). The IR absorption ranges associated with bulk carbonate and nitrate species are highlighted in blue and green, respectively.

**Carbonate and Nitrate Defects.** The HAp samples 2,3 and 5–7 (Table 2) were further characterized by infrared spectroscopy to study the influence of the synthesis protocols on the incorporation of carbonate species ($CO_3^{2-}$) in the crystalline structure. The latter species can be incorporated by substitution of the phosphate groups (B-type carbonates) and/or the hydroxide groups (A-type carbonates).[14] Such substitutions lead to the formation of complex materials $(Ca_{10-x-B}(HPO_4)_x(PO_4)_{6-x-B}(CO_3)_B(OH)_{2-x-B-2A}(CO_3)_A \cdot nH_2O, \quad 1.50 \leq Ca/P \leq 1.90)$.[13,14] Typically, the over-stoichiometry found for sample 2 ($Ca/P > 1.67$, Table 2) is associated with a substitution of the phosphates with type B carbonates.[62] The amounts of carbonates incorporated into the HAp structure appear to be greater for the syntheses performed at pH 9.0 compared to those carried out at pH 6.5 (Figure 7**b**). This observation is attributed to the introduction of ambient carbon dioxide into the reactor mainly *via* the ammonia sampling flask (section *Materials and Methods*) whose solubility is favored in alkaline media due to the formation of $HCO_3^-$ and $CO_3^{2-}$ species. Thus, the stabilization of the reaction medium at pH 9.0 during precipitation requires the addition of a larger volume of the ammonia solution, enriched in dissolved carbon dioxide, compared to that needed to maintain the reaction medium at pH 6.5. Nitrate incorporation in HAps, scarcely reported in earlier studies,[63,64] is also observed in samples prepared at basic pH (Figure 7**b**). The absence of conclusive data on their bulk location in HAps precludes any further analysis of their potential influence on the Ca/P ratio. Complementary IR, and $^{13}C$ and $^{15}N$ NMR measurements together with the use of different calcium precursors

$(Ca(NO_3)_2 \cdot 4H_2O, Ca(OH)_2$ or $CaCl_2)$ may help to provide further insights into the preferential location of these species and revisit the IR assignment of A- and B-type carbonates and nitrates in co-precipitated HAps. As mentioned by Elliott "the concept that the $CO_3^{2-}$ (and $NO_3^-$) ions were in two well-defined environments in precipitated HAps from aqueous systems was early recognised to be an over-simplification because of the multiple bands sometimes seen in the region of synthetic HAps (Figure 7**b**) and because of inconsistencies in the relative intensities of the IR bands in the spectra of synthetic HAps and the polarised spectrum of enamel".[14] These complementary data may allow to discuss the influence of the preparation conditions on the different possible carbonate substitutions in aqueous systems and to propose mechanisms for their introduction in line with the HAp precipitation pathways unravelled in the present work.

**CONCLUSIONS**

The model and experimental kinetic approaches used in the present work to investigate the competitive precipitation of CaPs, and their coupling with our earlier thermodynamic study,[28] allowed us to elucidate the pathways involved in the formation of synthetic HAps in open systems (dropwise syntheses). These precipitation pathways were elucidated and validated experimentally by *in situ* Raman spectroscopy and the implementation of original syntheses under kinetic control enabled the isolation of metastable CaPs. The formation of the ACP or OCP intermediates was found to be strongly dependent on the co-precipitation conditions (pH, temperature of the reaction medium and order of introduction of the precursor solution into the reactor). With respect to these precipitation pathways, it was possible to rationalize the incorporation of hydrogen phosphate and carbonate crystallographic defects in the mineral structure and the observed changes in textural properties (morphology and SSA) of the synthetic HAps. On this basis, this work also allowed to

rationalize earlier literature data. The main findings of the present study can be summarized as follows:

- At stationary pH and for open system syntheses, HAp is formed *via* the OCP phase at pH 6.5 and *via* the ACP phase at pH 9.0.

- The formation of HAp crystallites with a platelet morphology can occur if they are derived from the OCP phase, which had had sufficient time to grow before being hydrolyzed to HAp.

- The incorporation of $HPO_4^{2-}$ defects in the HAp structure is favored when this mineral component is formed *via* the OCP phase, which obviously intrinsically exhibits such groups in its perfect crystal structure.

Finally, the present study can serve as a basis to assist researchers in choosing synthesis parameters most appropriate to prepare targeted HAp materials with adequate SSA, morphology, and crystallographic defect content based on the considered application in materials science. Since the various chemical pathways should also impact the surface properties of HAp to a significant extent, as will be emphasized in a forthcoming paper, the control of the HAp preparation also appears to be a critical point for the design of HAp-based catalysts.


ASSOCIATED CONTENT

Supporting information on the synthesis and characterization of materials as well as mathematical details on the developed kinetic model are available free of charge via the Internet at

- Synthesis complementary information (Figures S1 and S2)

- Indexation of the XRD lines and Raman bands of CaPs (Tables S1 and S2)

- Homogeneous nucleation model (Figure S3)

- *In situ* Raman spectroscopy (Figure S4)

- Low-angles diffraction patterns (Figure S5)

- Critical analysis of earlier literature studies

AUTHOR CONTRIBUTIONS

Study conception and design: Guylène Costentin, Corentin Reynaud

Acquisition of data: Corentin Reynaud

Analysis and interpretation of data: Guylène Costentin, Corentin Reynaud, Cyril Thomas

Drafting of manuscript: Corentin Reynaud

Critical revision: Guylène Costentin, Cyril Thomas

**REFERENCES**

(1)     Schrödter, K.; Bettermann, G.; Staffel, T.; Wahl, F.; Klein, T.; Hofmann, T. Phosphoric Acid and Phosphates. In *Ullmann's Encyclopedia of Industrial Chemistry*; American Cancer Society, 2008.

(2)     Kibby, C. L.; Hall, W. K. Dehydrogenation of Alcohols and Hydrogen Transfer from Alcohols to Ketones over Hydroxyapatite Catalysts. *J. Catal.* **1973**, *31* (1), 65–73.

(3)     Tsuchida, T.; Yoshioka, T.; Sakuma, S.; Takeguchi, T.; Ueda, W. Synthesis of Biogasoline from Ethanol over Hydroxyapatite Catalyst. *Ind. Eng. Chem. Res.* **2008**, *47* (5), 1443–1452.

(4)     Tsuchida, T.; Kubo, J.; Yoshioka, T.; Sakuma, S.; Takeguchi, T.; Ueda, W. Reaction of Ethanol over Hydroxyapatite Affected by Ca/P Ratio of Catalyst. *J. Catal.* **2008**, *259* (2), 183–189.

(5)     Eagan, N. M.; Lanci, M. P.; Huber, G. W. Kinetic Modeling of Alcohol Oligomerization over Calcium Hydroxyapatite. *ACS Catal.* **2020**, *10* (5), 2978–2989.

(6)     Mohd Pu'ad, N. A. S.; Abdul Haq, R. H.; Mohd Noh, H.; Abdullah, H. Z.; Idris, M. I.; Lee, T. C. Synthesis Method of Hydroxyapatite: A Review. *Mater. Today Proc.* **2020**, *29*, 233–239.

(7)     Fihri, A.; Len, C.; Varma, R. S.; Solhy, A. Hydroxyapatite: A Review of Syntheses, Structure and Applications in Heterogeneous Catalysis. *Coord. Chem. Rev.* **2017**, *347*, 48–76.

(8)     Zhu, R.; Yu, R.; Yao, J.; Wang, D.; Ke, J. Morphology Control of Hydroxyapatite through Hydrothermal Process. *J. Alloys Compd.* **2008**, *457* (1), 555–559.

(9)     Xia, W.; Lin, K.; Gou, Z.; Engqvist, H. Morphology Control of Hydroxyapatite Crystal and Its Aggregates; Nova Science Publishers, 2012.

(10)    He, W.; Fu, Y.; Andersson, M. Morphological Control of Calcium Phosphate Nanostructures Using Lyotropic Liquid Crystals. *J. Mater. Chem. B* **2014**, *2* (21), 3214–3220.

(11)    Pai, S.; M Kini, S.; Selvaraj, R.; Pugazhendhi, A. A Review on the Synthesis of Hydroxyapatite, Its Composites and Adsorptive Removal of Pollutants from Wastewater. *J. Water Process Eng.* **2020**, *38*, 101574.

(12)    Betts, F.; Posner, A. S. An X-Ray Radial Distribution Study of Amorphous Calcium Phosphate. *Mater. Res. Bull.* **1974**, *9*, 353–360.

(13)    Chapter 3 - Hydroxyapatite and Nonstoichiometric Apatites. In *Studies in Inorganic Chemistry*; Elliott, J. C., Ed.; Structure and Chemistry of the Apatites and Other Calcium Orthophosphates; Elsevier, 1994; Vol. 18, pp 111–189.

(14)    Chapter 4 - Mineral, Synthetic and Biological Carbonate Apatites. In *Studies in Inorganic Chemistry*; Elliott, J. C., Ed.; Structure and Chemistry of the Apatites and Other Calcium Orthophosphates; Elsevier, 1994; Vol. 18, pp 191–304.

(15)    Rey, C.; Combes, C.; Drouet, C.; Glimcher, M. J. Bone Mineral: Update on Chemical Composition and Structure. *Osteoporos. Int.* **2009**, *20* (6), 1013–1021.

(16)    Raynaud, S.; Champion, E.; Bernache-Assollant, D.; Thomas, P. Calcium Phosphate Apatites with Variable Ca/P Atomic Ratio I. Synthesis, Characterisation and Thermal Stability of Powders. *Biomaterials* **2002**, *23* (4), 1065–1072.

(17)    Tsuchida, T.; Sakuma, S.; Takeguchi, T.; Ueda, W. Direct Synthesis of n-Butanol from Ethanol over Nonstoichiometric Hydroxyapatite. *Ind. Eng. Chem. Res.* **2006**, *45* (25), 8634–8642.

(18)    Matsumura, Y.; B. Moffat, J. Methanol Adsorption and Dehydrogenation over Stoichiometric and Non-Stoichiometric Hydroxyapatite Catalysts. *J. Chem. Soc. Faraday Trans.* **1996**, *92* (11), 1981–1984.

(19)    Mori, K.; Yamaguchi, K.; Hara, T.; Mizugaki, T.; Ebitani, K.; Kaneda, K. Controlled Synthesis of Hydroxyapatite-Supported Palladium Complexes as Highly Efficient Heterogeneous Catalysts. *J. Am. Chem. Soc.* **2002**, *124* (39), 11572–11573.

(20)    Ardanova, L. I.; Get'man, E. I.; Loboda, S. N.; Prisedsky, V. V.; Tkachenko, T. V.; Marchenko, V. I.; Antonovich, V. P.; Chivireva, N. A.; Chebishev, K. A.; Lyashenko, A. S. Isomorphous Substitutions of Rare Earth Elements for Calcium in Synthetic Hydroxyapatites. *Inorg. Chem.* **2010**, *49* (22), 10687–10693.

(21)    Bigi, A.; Boanini, E.; Gazzano, M. 7 - Ion Substitution in Biological and Synthetic Apatites. In *Biomineralization and Biomaterials*; Aparicio, C., Ginebra, M.-P., Eds.; Woodhead Publishing: Boston, 2016; pp 235–266.

(22)    Ibrahim, M.; Labaki, M.; Giraudon, J.-M.; Lamonier, J.-F. Hydroxyapatite, a Multifunctional Material for Air, Water and Soil Pollution Control: A Review. *J. Hazard. Mater.* **2020**, *383*, 121139.

(23)    Cawthray, J. F.; Creagh, A. L.; Haynes, C. A.; Orvig, C. Ion Exchange in Hydroxyapatite with Lanthanides. *Inorg. Chem.* **2015**, *54* (4), 1440–1445.

(24)    Ye, W.; Wang, X.-X. Ribbon-like and Rod-like Hydroxyapatite Crystals Deposited on Titanium Surface with Electrochemical Method. *Mater. Lett.* **2007**, *61* (19), 4062–4065.

(25)    Neira, I. S.; Kolen'ko, Y. V.; Lebedev, O. I.; Van Tendeloo, G.; Gupta, H. S.; Guitián, F.; Yoshimura, M. An Effective Morphology Control of Hydroxyapatite Crystals via Hydrothermal Synthesis. *Cryst. Growth Des.* **2009**, *9* (1), 466–474.

(26)    Yang, H.; Wang, Y. Morphology Control of Hydroxyapatite Microcrystals: Synergistic Effects of Citrate and CTAB. *Mater. Sci. Eng. C* **2016**, *62*, 160–165.

(27)    Martins, M. A.; Santos, C.; Almeida, M. M.; Costa, M. E. V. Hydroxyapatite Micro- and Nanoparticles: Nucleation and Growth Mechanisms in the Presence of Citrate Species. *J. Colloid Interface Sci.* **2008**, *318* (2), 210–216.

(28)    Reynaud, C.; Thomas, C.; Casale, S.; Nowak, S.; Costentin, G. Development of a Thermodynamic Approach to Assist the Control of the Precipitation of Hydroxyapatites and Associated Calcium Phosphates in Open Systems. *CrystEngComm* **2021**, *23* (27), 4857–4870.

(29)    Diallo-Garcia, S.; Ben Osman, M.; Krafft, J.-M.; Casale, S.; Thomas, C.; Kubo, J.; Costentin, G. Identification of Surface Basic Sites and Acid–Base Pairs of Hydroxyapatite. *J. Phys. Chem. C* **2014**, *118* (24), 12744–12757.

(30)    Nielsen, A. E. *Kinetics of Precipitation*; Pergamon Press; [distributed in the Western Hemisphere by Macmillan, New York], 1964.

(31)    Dirksen, J. A.; Ring, T. A. Fundamentals of Crystallization: Kinetic Effects on Particle Size Distributions and Morphology. *Chem. Eng. Sci.* **1991**, *46* (10), 2389–2427.

(32)    Cheng, P.-T. Octacalcium Phosphate Formationin Vitro: Implications for Bone Formation. *Calcif. Tissue Int.* **1985**, *37* (1), 91–94.

(33)    Brown, W. E.; Eidelman, N.; Tomazic, B. Octacalcium Phosphate as a Precursor in Biomineral Formation. *Adv. Dent. Res.* **1987**, *1* (2), 306–313.

(34)    Johnsson, M. S.-A.; Nancollas, G. H. The Role of Brushite and Octacalcium Phosphate in Apatite Formation. *Crit. Rev. Oral Biol. Med.* **1992**, *3* (1), 61–82.

(35)    Nancollas, G. H.; Wu, W. Biomineralization Mechanisms: A Kinetics and Interfacial Energy Approach. *J. Cryst. Growth* **2000**, *211* (1), 137–142.

(36)    Habraken, W. J. E. M.; Tao, J.; Brylka, L. J.; Friedrich, H.; Bertinetti, L.; Schenk, A. S.; Verch, A.; Dmitrovic, V.; Bomans, P. H. H.; Frederik, P. M.; Laven, J.; van der Schoot, P.; Aichmayer, B.; de With, G.; DeYoreo, J. J.; Sommerdijk, N. A. J. M. Ion-Association Complexes Unite Classical and Non-Classical Theories for the Biomimetic Nucleation of Calcium Phosphate. *Nat. Commun.* **2013**, *4* (1), 1507.

(37)    Wu, W.; Nancollas, G. H. Determination of Interfacial Tension from Crystallization and Dissolution Data: A Comparison with Other Methods. *Adv. Colloid Interface Sci.* **1999**, *79* (2), 229–279.

(38)    Tang, R.; Wu, W.; Haas, M.; Nancollas, G. H. Kinetics of Dissolution of β-Tricalcium Phosphate. *Langmuir* **2001**, *17* (11), 3480–3485.

(39)    Volod'ko, L. V.; Huoah, L. T. The Vibrational Spectra of Aqueous Nitrate Solutions. *J. Appl. Spectrosc.* **1968**, *9* (4), 1100–1104.

(40)    Robin, M.; Euw, S. V.; Renaudin, G.; Gomes, S.; Krafft, J.-M.; Nassif, N.; Azaïs, T.; Costentin, G. Insights into OCP Identification and Quantification in the Context of Apatite Biomineralization. *CrystEngComm* **2020**, *22* (16), 2728–2742.

(41)    Stammeier, J. A.; Purgstaller, B.; Hippler, D.; Mavromatis, V.; Dietzel, M. In-Situ Raman Spectroscopy of Amorphous Calcium Phosphate to Crystalline Hydroxyapatite Transformation. *MethodsX* **2018**, *5*, 1241–1250.

(42)    Gadaleta, S. J.; Paschalis, E. P.; Betts, F.; Mendelsohn, R.; Boskey, A. L. Fourier Transform Infrared Spectroscopy of the Solution-Mediated Conversion of Amorphous Calcium Phosphate to Hydroxyapatite: New Correlations between X-Ray Diffraction and Infrared Data. *Calcif. Tissue Int.* **1996**, *58* (1), 9–16.

(43)    Graham, S.; Brown, P. W. Reactions of Octacalcium Phosphate to Form Hydroxyapatite. *J. Cryst. Growth* **1996**, *165* (1), 106–115.

(44)     Kim, S.; Ryu, H.-S.; Shin, H.; Jung, H. S.; Hong, K. S. In Situ Observation of Hydroxyapatite Nanocrystal Formation from Amorphous Calcium Phosphate in Calcium-Rich Solutions. *Mater. Chem. Phys.* **2005**, *91* (2), 500–506.

(45)     Correia, R. N.; Magalhães, M. C. F.; Marques, P. A. A. P.; Senos, A. M. R. Wet Synthesis and Characterization of Modified Hydroxyapatite Powders. *J. Mater. Sci. Mater. Med.* **1996**, *7* (8), 501–505.

(46)     Torrent-Burgues, J.; Rodriguez-Clemente, R. Hydroxyapatite Precipitation in a Semibatch Process. *Cryst. Res. Technol.* **2001**, *36* (8–10), 1075–1082.

(47)     Cunniffe, G. M.; O'Brien, F. J.; Partap, S.; Levingstone, T. J.; Stanton, K. T.; Dickson, G. R. The Synthesis and Characterization of Nanophase Hydroxyapatite Using a Novel Dispersant-Aided Precipitation Method. *J. Biomed. Mater. Res. A* **2010**, *95A* (4), 1142–1149.

(48)     Dhand, V.; Rhee, K. Y.; Park, S.-J. The Facile and Low Temperature Synthesis of Nanophase Hydroxyapatite Crystals Using Wet Chemistry. *Mater. Sci. Eng. C* **2014**, *36*, 152–159.

(49)     Kramer, E.; Podurgiel, J.; Wei, M. Control of Hydroxyapatite Nanoparticle Morphology Using Wet Synthesis Techniques: Reactant Addition Rate Effects. *Mater. Lett.* **2014**, *131*, 145–147.

(50)     Brown, W. E.; Smith, J. P.; Lehr, J. R.; Frazier, A. W. Octacalcium Phosphate and Hydroxyapatite: Crystallographic and Chemical Relations between Octacalcium Phosphate and Hydroxyapatite. *Nature* **1962**, *196* (4859), 1050–1055.

(51)     Nelson, D. G.; McLean, J. D. High-Resolution Electron Microscopy of Octacalcium Phosphate and Its Hydrolysis Products. *Calcif. Tissue Int.* **1984**, *36* (2), 219–232.

(52)     Tomazic, B. B.; Tung, M. S.; Gregory, T. M.; Brown, W. E. Mechanism of Hydrolysis of Octacalcium Phosphate. *Scanning Microsc.* **1989**, *3* (1), 119–127.

(53)     Christoffersen, J.; Christoffersen, M. R.; Kibalczyc, W.; Andersen, F. A. A Contribution to the Understanding of the Formation of Calcium Phosphates. *J. Cryst. Growth* **1989**, *94* (3), 767–777.

(54)     Sugiura, Y.; Horie, M. Fabrication of Silver-Doped Apatite Powders from Silver-Substituted Octacalcium Phosphate Powders via Solid–Solid Phase-Conversion Process. *Ceram. Int.* **2021**, *47* (18), 25614–25621.

(55)     Iijima, M.; Kamemizu, H.; Wakamatsu, N.; Goto, T.; Doi, Y.; Moriwaki, Y. Transition of Octacalcium Phosphate to Hydroxyapatite in Solution at pH 7.4 and 37°C. *J. Cryst. Growth* **1997**, *181* (1), 70–78.

(56)     Tseng, Y.-H.; Mou, C.-Y.; Chan, J. C. C. Solid-solid NMR Study of the Transformation of Octacalcium Phosphate to Hydroxyapatite: A Mechanistic Model for Central Dark Line Formation. *J. Am. Chem. Soc.* **2006**, *128* (21), 6909–6918.

(57) Rey, C.; Combes, C.; Drouet, C.; Grossin, D.; Bertrand, G.; Soulié, J. 1.11 Bioactive Calcium Phosphate Compounds: Physical Chemistry. In *Comprehensive Biomaterials II*; Ducheyne, P., Ed.; Elsevier: Oxford, 2017; pp 244–290.

(58) Terpstra, R. A.; Bennema, P. Crystal Morphology of Octacalcium Phosphate: Theory and Observation. *J. Cryst. Growth* **1987**, *82* (3), 416–426.

(59) Berry, E. E. The Structure and Composition of Some Calcium-Deficient Apatites. *J. Inorg. Nucl. Chem.* **1967**, *29* (2), 317–327.

(60) Boskey, A. L.; Posner, A. S. Conversion of Amorphous Calcium Phosphate to Microcrystalline Hydroxyapatite. A pH-Dependent, Solution-Mediated, Solid-Solid Conversion. *J. Phys. Chem.* **1973**, *77* (19), 2313–2317.

(61) Harries, J. E.; Hukins, D. W. L.; Holt, C.; Hasnain, S. S. Conversion of Amorphous Calcium Phosphate into Hydroxyapatite Investigated by EXAFS Spectroscopy. *J. Cryst. Growth* **1987**, *84* (4), 563–570.

(62) Ben Osman, M.; Krafft, J. M.; Millot, Y.; Averseng, F.; Yoshioka, T.; Kubo, J.; Costentin, G. Molecular Understanding of the Bulk Composition of Crystalline Nonstoichiometric Hydroxyapatites: Application to the Rationalization of Structure–Reactivity Relationships. *Eur. J. Inorg. Chem.* **2016**, 2709–2720.

(63) Islam, M.; Chandra Mishra, P.; Patel, R. Physicochemical Characterization of Hydroxyapatite and Its Application towards Removal of Nitrate from Water. *J. Environ. Manage.* **2010**, *91* (9), 1883–1891.

(64) Gafurov, M.; Biktagirov, T.; Yavkin, B.; Mamin, G.; Filippov, Y.; Klimashina, E.; Putlayev, V.; Orlinskii, S. Nitrogen-Containing Species in the Structure of the Synthesized Nano-Hydroxyapatite. *JETP Lett.* **2014**, *99* (4), 196–203.

**TABLE OF CONTENTS SYNOPSIS**
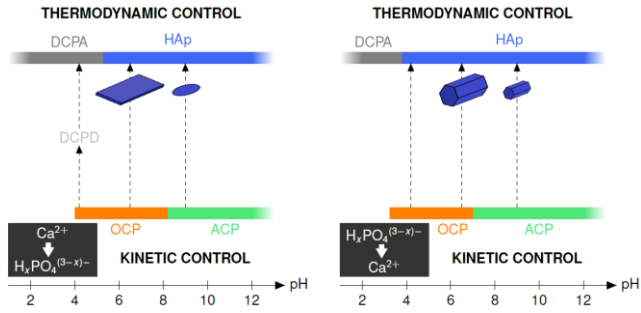


Schematic representation of the unraveled precipitation reaction pathways of calcium phosphates as a function of pH and the order of introduction of precursor ions into the synthesis reactor. The differences observed in textural and structural properties of the dropwise-synthetized thermodynamically-stable hydroxyapatite (HAp) can be accounted for by the formation of its kinetic octacalcium phosphate (OCP) or amorphous calcium phosphate (ACP) precursors, which could be identified unequivocally in dedicated kinetically controlled experiments.

# Supplementary Information for

# On the Comprehensive Precipitation of Hydroxyapatites Unraveled by a Combined Kinetic-Thermodynamic Approach

Corentin Reynaud,[1] Cyril Thomas,[1] and Guylène Costentin[1]*

*[1] Sorbonne Université, CNRS, Laboratoire de Réactivité de Surface (LRS), 4 place Jussieu,*

*75005 Paris, France*

*E-mail: guylene.costentin@sorbonne-universite.fr

This document includes:

**Synthesis complementary information**

**Automated reactor.**
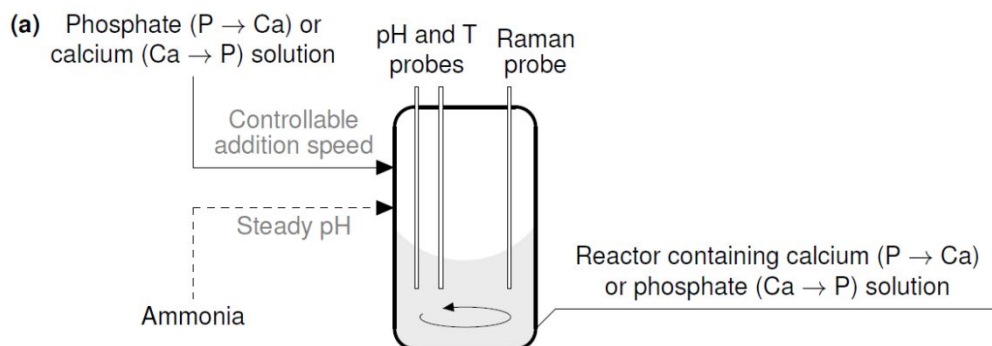


**Figure S1.** Schematic representation of the automated reactor used for the synthesis of the materials of this study and adapted with a Raman probe for *in situ* monitoring experiments (**a**) and photograph of the experimental setup (**b**).

**pH profiles.** During the kinetically-controlled syntheses, a fast addition rate of 50 mL/min of the precursor solution was used to shorten drastically the reaction time compared to that of the

thermodynamically-controlled syntheses (Table 2). The use of such a high addition rate makes it more difficult for the automated reactor to control the temperature at 37 or 80 °C and the pH at 6.5 or 9.0 (Figure S2**a**, **b**). By comparing the synthesis profiles of samples 7 (thermodynamic control, Figure S2**a**) and 15 (kinetic control, Figure S2**b**), we can observe that the temperature and the pH of the reaction medium varies from $80 \pm 1$ °C and $6.5 \pm 0.2$ to $74 \pm 7$ °C and $6.5 \pm 0.9$ for samples 7 and 15, respectively, during the addition stage. Given the limited impact of the temperature parameter on the nature of the precipitated thermodynamic products[1] and of the reaction intermediates as a function of the pH (Figure 1 and 2), it was considered that the lower accuracy with which the pH and temperature parameters were controlled by the automated reactor did not prevent the reliable identification of the nature of the intermediates. These data highlight, however, that the use of an automated reactor is of the greatest importance for such syntheses and that the absence of any control of the operating parameters may be at origin of the poorly-reproducible preparation of CaPs.
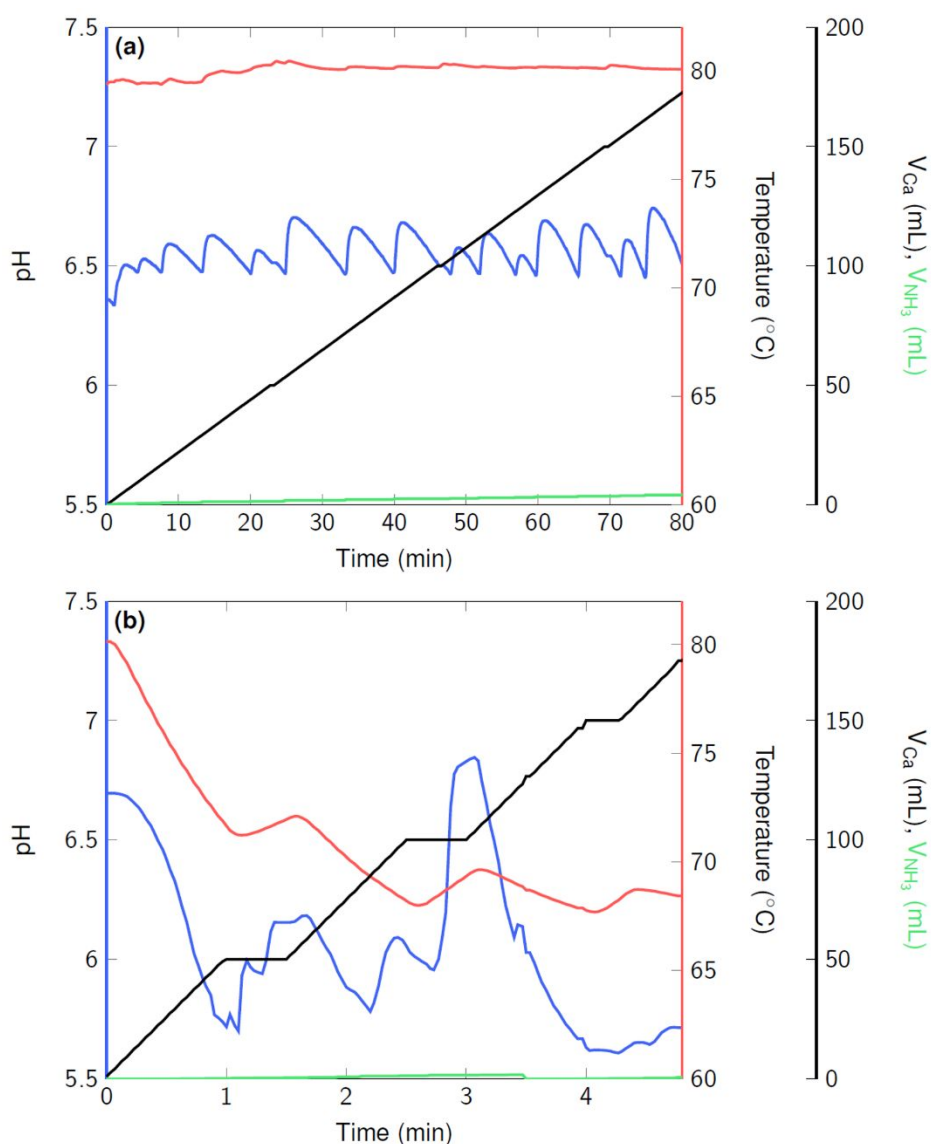
**Figure S2.** pH (blue) and temperature (red) profiles in the reactor during the addition step at 80 °C and pH 6.5 for an addition rate of 2.2 mL/min (**a**, Table 2, sample 7) or 50 mL/min (**b**, Table 2, sample E) of the calcium solution into the reactor containing the phosphate solution (Ca→P synthesis route). The pH control parameters are: mixing time = 12 s, minimum pH deviation = 0.02 and maximum pH rate = 0.3 pH unit/min.

## Indexation of the XRD lines and the Raman bands of CaPs

XRD and Raman techniques were complementary used (*i*) to identify the precipitated calcium phosphate(s) obtained after the washing/drying steps, (*ii*) to appreciate their crystallinity and (*iii*) to determine the origins of the sub-stoichiometry of HAps. Tables S1 and S2 list the assignment of the XRD and Raman contributions of the CaPs, respectively.

**Table S1.** XRD assignment of the diffraction lines below 40 ° for crystalline calcium phosphates: HAp (reference card n° 00-009-0432, ICDD), OCP (reference card n° 00-026-1056, ICDD), DCPD (reference card n° 00-009-0077) and DCPA (reference card n° 00-009-0080). The relative intensity (Int.) of each (h k l) diffraction line is indicated as a percentage of the most intense diffraction line.

| HAp | | | OCP | | | DCPD | | | DCPA | | |
|---|---|---|---|---|---|---|---|---|---|---|---|
| $2\theta$ (°) | (h k l) | Int. (%) | $2\theta$ (°) | (h k l) | Int. (%) | $2\theta$ (°) | (h k l) | Int. (%) | $2\theta$ (°) | (h k l) | Int. (%) |
| | | | 4.72 | (0 1 0) | 100 | | | | | | |
| | | | 9.44 | (0 2 0) | 15 | | | | | | |
| 10.82 | (1 0 0) | 12 | 9.77 | (1 1 0) | 13 | 11.68 | (0 2 0) | 100 | | | |
| | | | 14.51 | (1 -2 0) | 2 | | | | 13.12 | (0 1 0) | 14 |
| | | | 16.04 | (-1 0 1) | 8 | | | | | | |
| | | | 16.35 | (0 2 1) | 2 | | | | 16.31 | (1 0 0) | 4 |
| 16.84 | (1 0 1) | 6 | 17.00 | (1 -1 1) | 1 | | | | | | |
| | | | 17.37 | (-1 1 1) | 4 | 17.98 | (-1 1 1) | 2 | 17.76 | (0 -1 1) | 4 |
| | | | 18.41 | (1 -3 0) | 2 | | | | | | |
| 18.78 | (1 1 0) | 4 | 18.84 | (0 -3 1) | 2 | | | | | | |
| | | | 18.99 | (0 4 0) | 1 | | | | | | |
| | | | 19.65 | (0 3 1) | 3 | | | | 19.80 | (0 1 1) | 2 |
| | | | 19.75 | (-1 2 1) | 3 | | | | 20.26 | (-1 0 1) | 4 |
| | | | 20.67 | (1 3 1) | 2 | 20.93 | (0 2 1) | 100 | 20.79 | (1 -2 0) | 4 |
| 21.82 | (2 0 0) | 10 | 21.60 | (2 3 0) | 2 | | | | | | |
| | | | 22.67 | (1 -4 0) | 5 | | | | 22.04 | (1 0 1) | 4 |
| 22.90 | (1 1 1) | 10 | 22.91 | (2 0 1) | 4 | | | | | | |
| | | | 23.01 | (-2 0 1) | 3 | | | | | | |
| | | | 23.48 | (0 4 1) | 3 | 23.39 | (0 4 0) | 8 | | | |
| | | | 23.74 | (2 2 1) | 5 | 23.71 | (1 3 0) | < 1 | | | |
| | | | 24.30 | (-2 1 1) | 10 | 24.50 | (-1 3 1) | 2 | 24.03 | (1 -2 1) | 4 |
| 25.35 | (2 0 1) | 2 | 25.49 | (2 3 1) | 8 | | | | 25.58 | (-1 2 1) | 14 |
| 25.88 | (0 0 2) | 40 | 25.87 | (2 -2 1) | 17 | | | | | | |
| | | | 26.00 | (0 0 2) | 20 | | | | 26.43 | (0 2 0) | 70 |
| | | | 26.36 | (-2 2 1) | 6 | | | | 26.59 | (2 -2 0) | 75 |

| 2θ | hkl | I | 2θ | hkl | I | 2θ | hkl | I | 2θ | hkl | I |
|---|---|---|---|---|---|---|---|---|---|---|---|
| | | | 26.91 | (-1 -5 1) | 7 | | | | 26.75 | (2 -1 0) | 16 |
| | | | 27.18 | (1 -5 0) | 6 | | | | 27.00 | (0 0 2) | 10 |
| | | | 27.78 | (2 5 0) | 8 | | | | | | |
| 28.13 | (1 0 2) | 12 | 28.04 | (2 4 1) | 8 | | | | | | |
| | | | 28.47 | (-1 -2 2) | 3 | | | | 28.49 | (-1 -1 1) | 20 |
| 28.97 | (2 1 0) | 18 | 28.61 | (-1 1 2) | 2 | | | | 28.77 | (0 -1 2) | 6 |
| | | | 29.21 | (0 -3 2) | 5 | 29.26 | (0 4 1) | 75 | 29.90 | (-2 2 1) | 2 |
| | | | 29.60 | (3 3 0) | 3 | | | | 30.19 | (-1 1 2) | 100 |
| | | | 30.31 | (-1 2 2) | 5 | | | | 30.41 | (-1 0 2) | 35 |
| | | | 30.66 | (-1 5 1) | 4 | 30.51 | (-2 2 1) | 50 | 30.68 | (2 -1 1) | 4 |
| | | | 31.10 | (2 5 1) | 10 | | | | 31.02 | (0 2 1) | 8 |
| | | | 31.55 | (2 6 0) | 33 | 31.30 | (-1 1 2) | 10 | 31.17 | (1 1 1) | 4 |
| 31.77 | (2 1 1) | 100 | 31.70 | (2 -4 1) | 32 | 31.97 | (2 0 0) | 2 | 31.44 | (0 1 2) | 2 |
| 32.20 | (1 1 2) | 60 | 32.18 | (-1 -4 2) | 15 | | | | 32.38 | (1 -3 0) | 10 |
| | | | 32.59 | (3 3 1) | 12 | | | | 32.48 | (2 -3 0) | 20 |
| 32.90 | (3 0 0) | 60 | 33.06 | (0 4 2) | 8 | | | | 32.89 | (1 0 2) | 35 |
| | | | 33.52 | (0 7 0) | 17 | 33.54 | (1 5 0) | 4 | | | |
| 34.05 | (2 0 2) | 25 | 33.97 | (1 -6 1) | 12 | 33.82 | (1 3 1) | 4 | | | |
| | | | 34.24 | (3 -3 0) | 7 | 34.15 | (2 2 0) | 50 | | | |
| | | | 34.38 | (2 -2 2) | 7 | 34.43 | (-2 0 2) | 30 | | | |
| | | | 34.92 | (-1 6 1) | 5 | 35.11 | (0 0 2) | 4 | 34.73 | (2 -3 1) | 4 |
| 35.48 | (3 0 1) | 6 | 35.25 | (-1 -7 1) | 4 | 35.42 | (0 6 0) | 2 | 35.42 | (-1 2 2) | 4 |
| | | | 36.10 | (-2 -5 1) | 2 | 35.60 | (-1 3 2) | 4 | 35.91 | (0 -2 2) | 16 |
| | | | 36.27 | (0 5 2) | 3 | | | | 36.06 | (-1 -1 2) | 2 |
| | | | 36.53 | (1 -7 0) | 2 | 36.90 | (-2 4 1) | 14 | 36.76 | (2 0 1) | 2 |
| | | | 38.02 | (1 8 0) | 2 | 37.10 | (0 2 2) | 16 | 37.26 | (-2 1 2) | 2 |
| | | | 38.52 | (2 7 1) | 3 | | | | 38.25 | (2 -2 2) | 4 |
| 39.20 | (2 1 2) | 8 | 39.06 | (-3 0 2) | 2 | | | | 39.04 | (1 2 0) | 10 |
| | | | 39.65 | (3 6 1) | 2 | | | | 39.37 | (2 -1 2) | 2 |
| | | | 39.76 | (-1 -8 1) | 2 | 39.71 | (0 6 1) | 4 | | | |
| 39.82 | (3 1 0) | 20 | 39.89 | (0 6 2) | 2 | | | | | | |

**Table S2.** Raman shift and assignment of the vibrations of calcium phosphates, (CD)HAp, ACP, OCP, DCPD and DCPA extracted from earlier literature studies.[2–5]

| | (CD)HAp | ACP | OCP | DCPD | DCPA |
|---|---|---|---|---|---|
| $\nu_3(PO_4)$ or $\nu_3(HPO_4)$ stretch | | | | 1132 | 1131 |
| | | 1118 | 1112 $HPO_4^{2-}$ (hydrated layer) | 1119 | |
| | | | | | 1094 |
| | 1077 | | 1079 $PO_4^{3-}$ and $HPO_4^{2-}$ | 1079 | |
| | 1064 | | | 1061 | |
| | 1057 | | 1052 $PO_4^{3-}$ | | |
| | 1048 | 1050 | 1048 $PO_4^{3-}$ | | |
| | 1041 | | | | |
| | 1034 | | 1036 $PO_4^{3-}$ | | |
| | 1029 | | 1027 $PO_4^{3-}$ | | |
| $\nu_1(PO_4)$ or $\nu_1(HPO_4)$ stretch | 1011 $HPO_4^{2-}$ (CDHAp) | | 1011 $HPO_4^{2-}$ | | |
| | | | 1005 $HPO_4^{2-}$ | | |
| | | | | 986 | 988 |
| | 964–961 | | 966 $PO_4^{3-}$ | | |
| | | | 959 $PO_4^{3-}$ | | |
| | | 951 | | | |
| $HPO_4^{2-}$ [P–(OH)] stretch | 920 $HPO_4^{2-}$ (CDHAp) | | 916 (apatite layer) | | |
| | | | | | 900 |
| | 879 $HPO_4^{2-}$ (CDHAp) | | 874 (hydrated layer) | 878 | |
| $\nu_4(PO_4)$ or $\nu_4(HPO_4)$ bend | 614 | | 619 $PO_4^{3-}$ | | |
| | 607 | | 609 $PO_4^{3-}$ | | |
| | 591 | 594 | 591 $PO_4^{3-}$ and $HPO_4^{2-}$ | 588 | 588 |
| | 580 | | 577 $PO_4^{3-}$ and $HPO_4^{2-}$ | | 574 |
| | | | 556 $HPO_4^{2-}$ | | 563 |
| | | | 523 $HPO_4^{2-}$ | 525 | |
| $\nu_2(PO_4)$ or $\nu_2(HPO_4)$ bend | 448 | 451 | 451 $PO_4^{3-}$ | | |
| | 433 | | 427 $PO_4^{3-}$ | | |
| | | 419 | | | |
| | | | | | 420 |
| | | | 409 $HPO_4^{2-}$ | 411 | |
| | | | 353 $HPO_4^{2-}$ (hydrated layer) | 381 | 394 |

**Homogeneous nucleation model**

As developed in the manuscript for a perfect crystal of HAp, the same procedure led to the following supersaturation ratio equations for the other CaPs:

$$S^{ACP} = \left( \frac{a(Ca^{2+})_t^3 \, a(PO_4^{3-})_t^2}{K_s^{ACP}} \right)^{\frac{1}{3+2}} \qquad \text{(Eq. S1)}$$

$$S^{OCP} = \left( \frac{a(Ca^{2+})_t^4 \, a(PO_4^{3-})_t^3 \, a(H_3O^+)_t}{K_s^{OCP}} \right)^{\frac{1}{4+3+1+\frac{3}{2}}} \qquad \text{(Eq. S2)}$$

$$S^{DCPD} = \left( \frac{a(Ca^{2+})_t \, a(HPO_4^{2-})_t}{K_s^{DCCP}} \right)^{\frac{1}{1+1+2}} \qquad \text{(Eq. S3)}$$

Due to the acid-base properties of the $HPO_4^{2-}$, $PO_4^{3-}$ and $OH^-$ species constitutive of these ionic solids, the supersaturation ratio is greatly dependent on $pH$ (Figure S3). As expected, we can note that the more basic the $pH$ at the beginning of the precipitation reaction is, the higher this supersaturation ratio parameter is and the faster is the nucleation rate.
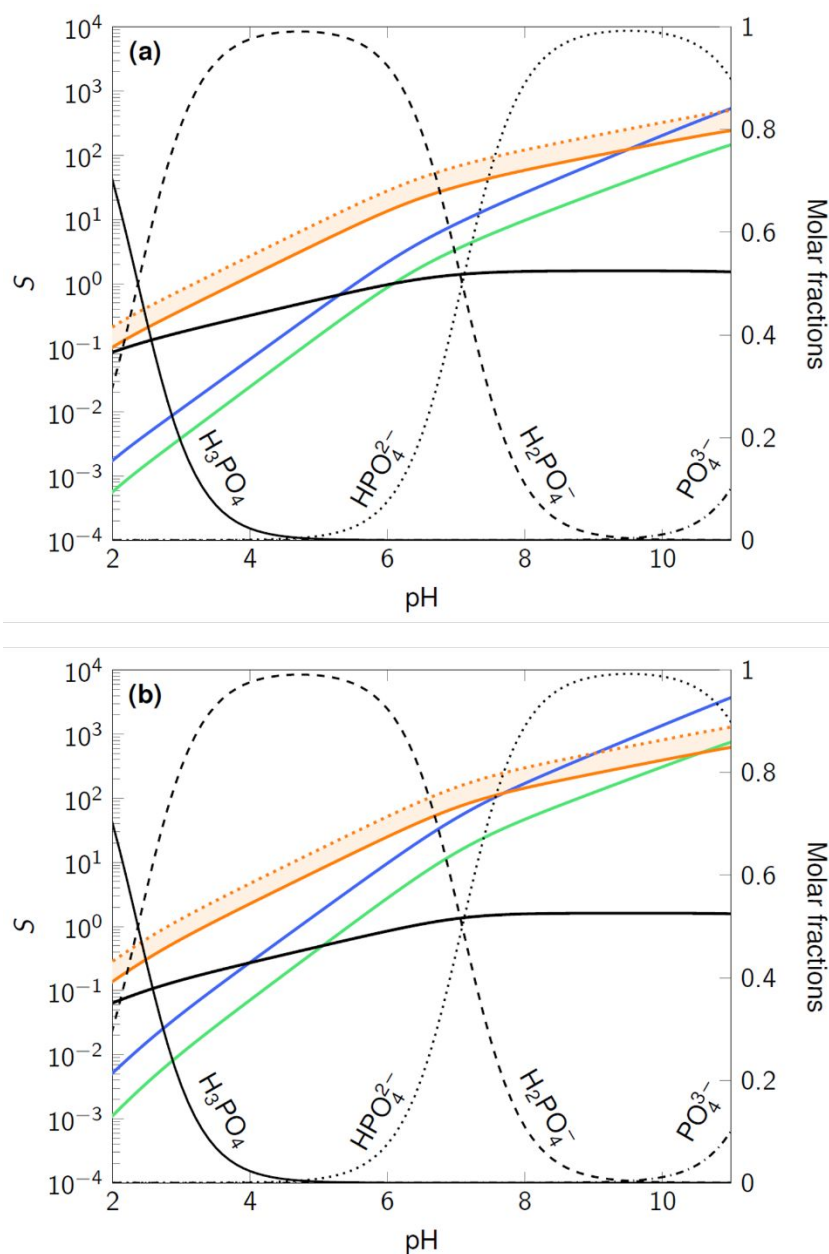
**Figure S3.** Supersaturation ratio $S$ calculated as a function of the pH of the reaction medium at 80 °C at the beginning of synthesis when a drop of the calcium solution is introduced into the reactor containing the phosphate solution (**a**, Ca→P, $[P]_0 = 0.13$ mol/L) or *vice versa* (**b**, P→Ca, $[Ca^{2+}]_0 = 0.22$ mol/L) for the precipitation of HAp, ACP, OCP and DCPD. For OCP, an area is plotted due to the uncertainty in the value of its solubility product at 80 °C (Table 1). Note that below pH 3–4, no nucleation is expected when the first drop is added as the condition $S > 1$ is not verified. The speciation of the phosphate species in aqueous solution at the equilibrium at 80 °C ($H_3PO_4$ (solid line), $H_2PO_4^-$ (dashed line), $HPO_4^{2-}$ (dotted line) and $PO_4^{3-}$ (dotdashed line)) is also plotted as a function of the pH of the reaction medium.

## *In situ* Raman spectroscopy
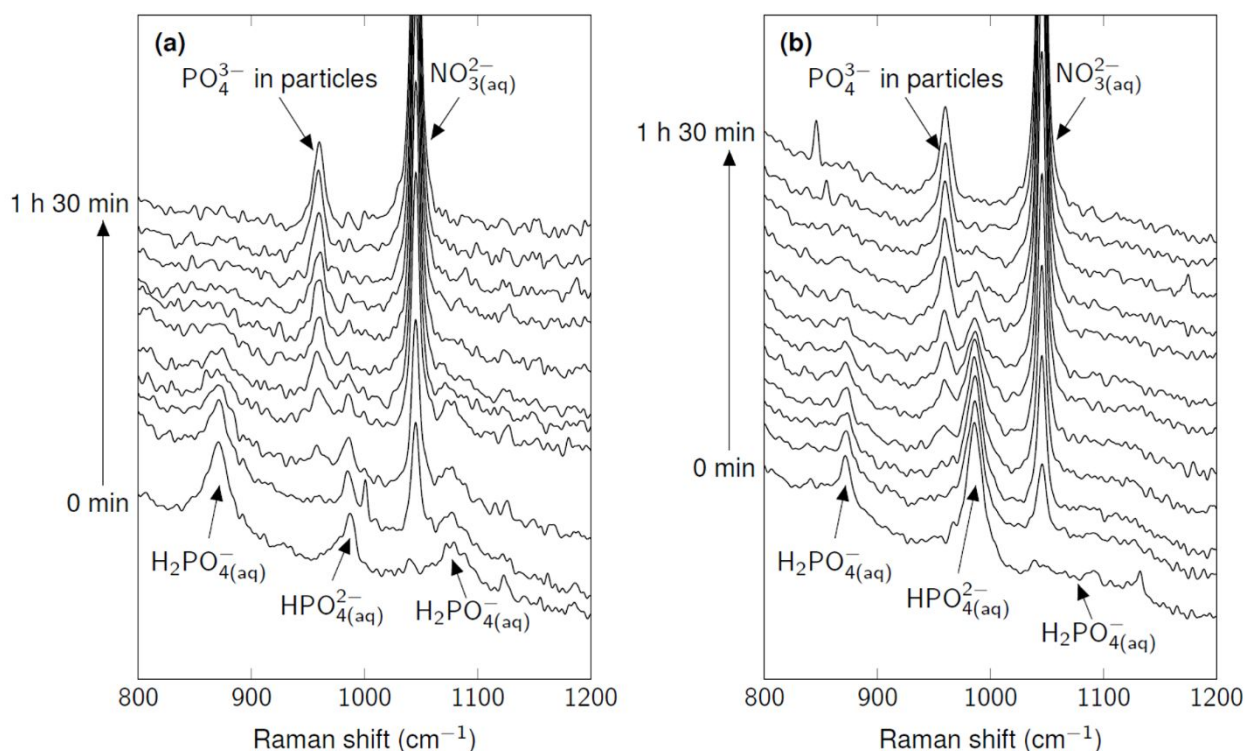


**Figure S4.** *In situ* monitoring of the CaPs precipitation by Raman spectroscopy during the addition step of the syntheses carried out at pH 6.5 (**a**) and 9.0 (**b**) following the Ca→P route at 80 °C with an addition rate of 2.2 mL/min. The spectrum at time 0 min is that recorded in the reaction medium initially containing the phosphate solution of initial concentration $[P]_0 = 0.13$ mol/L at pH 6.5 (**a**) and 9.0 (**b**). Absorption bands associated with dissolved ions in solution and with phosphate groups in the particles are indicated by arrows.

## Low-angle diffraction patterns

The diffraction patterns of samples B, D and F were acquired at low-angles (Figure S5). As observed on their high-angle diffraction patterns (Figure 4), samples D and F also show a diffraction peak at low angles around 4.72 ° attesting for the presence of OCP. In contrast, this low-angle peak is found to be absent from the diffraction pattern of sample B, whose synthesis did not lead to the initial formation of OCP, as predicted by the homogeneous nucleation model developed in the present study at pH 9.0 and 80 °C, but to that of ACP (Figure 4**a**, Table 2).
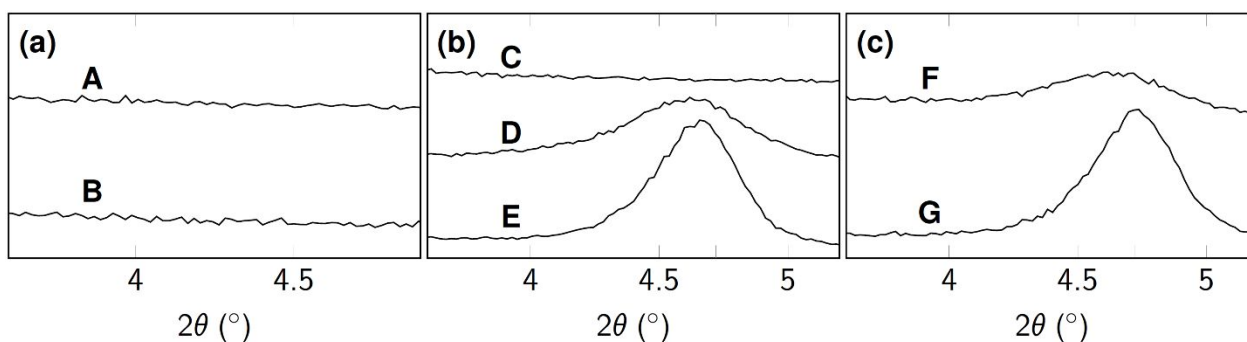
**Figure S5.** Low-angle diffraction patterns of samples A, B prepared at pH 9.0 (**a**), C–E prepared at pH 6.5 (**b**) and F, G prepared at pH 4.2 (**c**), which description is listed in Table 2. The contribution around 4.72° is characteristic of the OCP phase (Table S1).

**Critical analysis of earlier literature studies**

To the best of our knowledge, the influence of the pH of precipitation of CaPs, with the dropwise addition of a precursor solution into the other precursor solution, has been scarcely studied, as most of the data reported to date were collected in basic media. Correia *et al.* showed that the precipitation of HAp, following a P→Ca route (dropwise addition, no addition rate specified) at pH 8−10 (ammonia) and 50−75 °C followed by 4−6 days of ageing under the same pH and temperature conditions, led to particles with a rod-like shape and Ca/P ratios ranging from 1.62 to 1.66.[6] Similarly, Dhand *et al.* reported on the formation of HAp crystals with a "compact rice grain morphology" using a P→Ca route (addition rate : 3 mL/min) at pH 11 (ammonia) and 37 °C followed by an overnight maturation step.[7] Comparable morphologies have been reported also by Kramer *et al.* by studying the influence of addition rate on HAp precipitation. The use of synthesis conditions by these authors close to those of the present study (P→Ca route, 2.33 mL/min, pH 11−12 (ammonia, pH adjusted before addition only), 3 h of aging at 75 °C) "resulted in needle- or rod-shaped particles".[11] The synthesis conditions used in these studies[6–8] are found to be relatively close to those used in the present one to prepare sample 2 (Table 2), which exhibited a rod-like morphology (Figure 6**c**) and a Ca/P ratio of 1.72. The synthesis of rod-like HAp particles can be explained with regard to the proposed precipitation pathways in a basic medium (Figure 1), namely the formation of HAp via the initial precipitation of an amorphous precursor (ACP) rapidly hydrolyzed during the addition step.

Few studies have reported on the influence of the order of introduction of the precursors in a basic medium on the characteristics of the synthesized HAps.[9,10] Torrent-Burgues *et al.* showed that the P→Ca route (1 mL/min) at pH 9 (KOH) and 85 °C led to a stoichiometric HAp material (Ca/P $=$

11

1.67), while the Ca→P route led to CDHAp (Ca/P = 1.53).[9] Samples 2 (P→Ca) and 3 (Ca→P) synthesized in the present study under similar conditions (Table 2) exhibited Ca/P ratios of 1.72 and 1.66, respectively. The noticeable differences in Ca/P ratio (1.67/1.72 and 1.53/1.66) may be essentially attributed to the presence of B-type carbonates in our samples (Figure 7**b**), which were not incorporated in the materials prepared by Torrent-Burgues *et al.* due to the use of an $N_2$ atmosphere and a KOH solution that could be degassed (unlike our ammonia solution). Overall, the use of the P→Ca synthesis route is found to favor the formation of calcium-enriched HAps compared to those synthesized by the Ca→P route. The influence of the synthesis route, which was not discussed by Lu and Leng,[12] can be accounted for by a common ion effect (calcium or phosphate type) on the kinetics of ACP hydrolysis to HAp in a basic medium (Figure 1). In the P→Ca route, ACP particles nucleate at the beginning of the addition step in a calcium-rich solution favouring their hydrolysis into HAp (Eq. 5). At the end of the synthesis, the HAp particles should likely reach a more advanced stage of hydrolysis (and therefore a higher Ca/P ratio) than if they had nucleated in a solution rich in phosphates (Ca→P route) that should have hardly any influence on the hydrolysis kinetics. Cunniffe *et al.* reported that the Ca→P synthesis route led to smaller HAp particles compared to those obtained by the P→Ca route in a basic medium.[13] The smaller HAp crystallites observed for sample 3 compared to those obtained in sample 2 in the present study (Figure 6**c**, **d**) are therefore consistent with the earlier findings of Cunniffe *et al.*[13] As the progressive addition of the phosphate solution into the reactor containing the calcium solution favours the rapid hydrolysis of the ACP nuclei into HAp ones, it is anticipated that the growth process of the HAp nuclei should be favoured during the addition step in the P→Ca route (sample 2) compared to the Ca→P route (sample 3) and should lead to larger particles with a better-defined morphology in the former sample.

At pH 6.5, no synthesis with a protocol close to that used in this study (dropwise addition) has been described in the literature, as batch syntheses are most often implemented.

## References

(1) Reynaud, C.; Thomas, C.; Casale, S.; Nowak, S.; Costentin, G. Development of a Thermodynamic Approach to Assist the Control of the Precipitation of Hydroxyapatites and Associated Calcium Phosphates in Open Systems. *CrystEngComm* **2021**, *23* (27), 4857–4870.

(2) Blakeslee, K. C.; Condrate, R. A. Vibrational Spectra of Hydrothermally Prepared Hydroxyapatites. *J. Am. Ceram. Soc.* **1971**, *54*, 559–563.

(3) Stammeier, J. A.; Purgstaller, B.; Hippler, D.; Mavromatis, V.; Dietzel, M. In-Situ Raman Spectroscopy of Amorphous Calcium Phosphate to Crystalline Hydroxyapatite Transformation. *MethodsX* **2018**, *5*, 1241–1250.

(4) Fowler, B. O.; Marković, M.; Brown, W. Octacalcium Phosphate. 3. Infrared and Raman Vibrational Spectra. *Chem. Mater.* **1993**, *5*, 1417–1423.

(5) Xu, J.; Butler, I. S.; Gilson, D. F. R. FT-Raman and High-Pressure Infrared Spectroscopic Studies of Dicalcium Phosphate Dihydrate ($CaHPO_4 \cdot 2H_2O$) and Anhydrous Dicalcium Phosphate ($CaHPO_4$). *Spectrochim. Acta Part Mol. Spectrosc.* **1999**, *55*, 2801–2809.

(6) Correia, R. N.; Magalhães, M. C. F.; Marques, P. A. A. P.; Senos, A. M. R. Wet Synthesis and Characterization of Modified Hydroxyapatite Powders. *J. Mater. Sci. Mater. Med.* **1996**, *7* (8), 501–505.

(7) Dhand, V.; Rhee, K. Y.; Park, S.-J. The Facile and Low Temperature Synthesis of Nanophase Hydroxyapatite Crystals Using Wet Chemistry. *Mater. Sci. Eng. C* **2014**, *36*, 152–159.

(8) Kramer, E.; Podurgiel, J.; Wei, M. Control of Hydroxyapatite Nanoparticle Morphology Using Wet Synthesis Techniques: Reactant Addition Rate Effects. *Mater. Lett.* **2014**, *131*, 145–147.

(9) Torrent-Burgues, J.; Rodriguez-Clemente, R. Hydroxyapatite Precipitation in a Semibatch Process. *Cryst. Res. Technol.* **2001**, *36* (8–10), 1075–1082.

(10) Cunniffe, G. M.; O'Brien, F. J.; Partap, S.; Levingstone, T. J.; Stanton, K. T.; Dickson, G. R. The Synthesis and Characterization of Nanophase Hydroxyapatite Using a Novel Dispersant-Aided Precipitation Method. *J. Biomed. Mater. Res. A* **2010**, *95A* (4), 1142–1149.